

Seismic behavior of stiffened concrete-filled double-skin tubular columns

B. Shekastehband^{*}, S. Mohammadbagheri^a and A. Taromi^b

Civil Engineering Department, Urmia University of Technology, Urmia, Iran

(Received August 18, 2017, Revised December 14, 2017, Accepted March 28, 2018)

Abstract. The imperfect steel-concrete interface bonding is an important deficiency of the concrete-filled double skin tubular (CFDST) columns that led to separating concrete and steel surfaces under lateral loads and triggering buckling failure of the columns. To improve this issue, it is proposed in this study to use longitudinal and transverse steel stiffeners in CFDST columns. CFDST columns with different patterns of stiffeners embedded in the interior or exterior surfaces of the inner or outer tubes were analyzed under constant axial force and reversed cyclic loading. In the finite element modeling, the confinement effects of both inner and outer tubes on the compressive strength of concrete as well as the effect of discrete crack for concrete fracture were incorporated which give a realistic prediction of the seismic behavior of CFDST columns. Lateral strength, stiffness, ductility and energy absorption are evaluated based on the hysteresis loops. The results indicated that the stiffeners had determinant role on improving pinching behavior resulting from the outer tube's local buckling and opening/closing of the major tensile crack of concrete. The lateral strength, initial stiffness and energy absorption capacity of longitudinally stiffened columns with fixed-free end condition were increased by as much as 17%, 20% and 70%, respectively. The energy dissipation was accentuated up to 107% for fixed-guided end condition. The use of transverse stiffeners at the base of columns increased energy dissipation up to 35%. Axial load ratio, hollow ratio and concrete strength affecting the initial stiffness and lateral strength, had negligible effect of the energy dissipation of the columns. It was also found that the longitudinal stiffeners and transverse stiffeners have, respectively, negative and positive effects on ductility of CFDST columns. The conclusions, drawn from this study, can in turn, lead to the suggestion of some guidelines for the design of CFDST columns.

Keywords: CFDST columns; longitudinal stiffeners; transverse ring stiffeners; cyclic loading; hysteresis; pinching; ductility; dissipated energy

1. Introduction

Composite steel-concrete construction has become a widespread solution in modern construction. It ideally combines the advantages of both steel and concrete, namely fast construction, high strength and light weight of steel together with inherent mass, stiffness, damping and economy of concrete. A creative innovation of composite steel-concrete construction is the concrete-filled double skin steel tube (CFDST) which consists of two concentric steel tubes with the confined concrete sandwiched in between. CFDST optimally combines the benefits of traditional concrete-filled steel tube (CFST), and a sandwich form resulting in higher section modulus, higher bending stiffness, enhanced stability under external pressure, better damping characteristics, and improved cyclic performance (Han *et al.* 2006, Tao *et al.* 2004, Kim *et al.* 2013, Ren *et al.* 2014, Romero *et al.* 2015).

In the literature, some specific performance features of CFDSTs, such as flexural stiffness, ductility and energy dissipation capacity subjected to cyclic loading have been

studied (Lin and Tsai 2001, Elchalakani *et al.* 2002, Zhao *et al.* 2002). Experimental studies showed that short CFDST columns have the best performance among different short columns such as steel SHS, CFST made of SHS and double skin steel tubes made of SHS as the outer tube and CHS as the inner tube where the annulus between the tubes was partly filled with concrete in the lower part as the tube under cyclic loading (Nakanishi *et al.* 1999). However, steel tubes in slender CFDST columns are vulnerable to local buckling which increases with decreasing thickness. Therefore, ductility of CFDSTs as well as their ability to dissipate energy decreases when subjected to earthquake actions.

Experiments to evaluate the response of simply supported CFDST beam-columns under constant axial load and cyclically increasing flexural loading showed that the failure features of CFDST specimens under cyclic loading are very similar to those of CFST columns. The columns failed due to tensile fracture at the bulge location, accompanied with a sudden drop in the lateral load bearing capacity. In general, the ductility and energy dissipation ability of specimens with circular sections are higher than those of the specimens with square sections (Han *et al.* 2006). Based on the theoretical model, it was found that the ultimate lateral load increases as the nominal steel ratio, strength of outer steel tube or concrete strength increases. Further increase in the axial load level reduces the ultimate

*Corresponding author, Assistant Professor,
E-mail: b.shekastehband@uut.ac.ir

^a M.Sc.

^b M.Sc.

lateral load (Han *et al.* 2009). Cyclic loading tests on concrete-filled double-skin (SHS outer and CHS inner) stainless steel tubular beam-columns showed that the axial load level and thickness of outer tubes have a primary influence on the behavior of the test specimens. However, the hollowness ratio and the concrete strength have a little effect when the axial load level is low (Zhou and Xu 2016). Even though, use of high-strength materials may cause the great benefits of CFDSTs in terms of strength and stiffness, their main disadvantage leading to lower ductility is not desirable under seismic actions.

Along with their benefits, CFDST columns have some drawbacks stemming from the inadequate steel-concrete interface bonding, which would entail improving interface interaction as well as postponing overall buckling (Shekastehband *et al.* 2017). The efficiency of the confinement and interaction enhancing the overall strength and ductility of the columns was shown to be dependent on the shape of the steel tubes (Han *et al.* 2011).

There are limited researches about structural integrity between tubes and concrete (Ahmed *et al.* 2005) while the slippage between them might potentially be caused by bending deformation. Investigation through the literature reflects that the confinement is substantially reduced for square outer columns, and the failure mode of the outer tube involved outward local buckling, involving separation of the tube from the concrete core (Hassanein *et al.* 2015).

Recent researches conducted on the seismic behavior of CFDST columns showed that the performance depended on the geometric properties of the outer tube and concrete core, with the ultimate cyclic capacity increasing significantly with an increase in the strength and thickness of the outer tube and concrete core (Han *et al.* 2009).

Questions arise as to whether or not economical an increase in the strength/thickness of the components such as concrete core. How can be increased the confining pressure provided to the concrete in these columns? How can be increased the performance characteristics of these columns subjected to seismic excitation?

Retrofitting and improving the steel-concrete interface interaction have been studied by some researchers. Welding shear connectors at the interface between tubes and concrete core (Shimizu *et al.* 2013), employing steel rings restricting the dilation of outer steel tube (Dong and Ho 2012, Ho and Dong 2014) or utilizing FRP wraps around the concrete core (Talaieitaba *et al.* 2015) are some strategies proposed to improve the strength and the ductility of CFDST columns.

Although a lot of researches were conducted on mechanical performance of the CFDST columns, the necessity of stiffeners to compensate the imperfect steel-concrete interface bonding as well as postponing local buckling in the CFDST columns under seismic actions has not been addressed. It is expected that longitudinal stiffeners and transverse stiffeners may aid in perfect bonding of the in-filled concrete to the steel tubes which may increase lateral strength and ductility as well as energy dissipation capacity of the CFDST columns. Moreover, it should be mentioned that FE modeling of these columns, specifically considering the crack propagation and its subsequent effects on the hysteretic behavior is a

cumbersome and tedious task. This issue reflects the need in an exhaustive attention in simulating of tensile cracks. The in-filled concrete of CFDST column is often modeled using concrete damage plasticity. However, the drawback of the model in simulating accurate tensile cracking in concrete can be resolved by including of the discrete crack model at the location of the major tensile crack (Goto *et al.* 2010, Imani *et al.* 2014). Therefore, the main aims of the present study are:

- (1) to examine the nonlinear cyclic behavior of stiffened CFDST columns while inclusion of the discrete crack model for the sandwiched concrete;
- (2) to evaluate the effect of stiffeners type on the performance characteristics of the columns;
- (3) to evaluate the effect of important parameters such as load level, end-condition, hollow section ratio and concrete strength on the hysteretic behavior.

2. Finite element modeling

2.1 General

The typical floor plan of the 3-story buildings considered in the design of CFDST columns is depicted in Fig. 1. The overall dimensions of the floor plan were presumed to be $20 \times 20 \text{ m}^2$. To assess the individual columns performance against seismic action, a critical column at the possible location, as shown in Fig. 1, is considered in this study. However, results of this local model stage may in turn be used to assess the overall response of the structure due to failure of the critical columns.

One end fixed and one end free boundary conditions is assigned for the column. The axial and lateral loads are applied at the column top as illustrated in Fig. 2. In design process the attainment of material strength is assumed for all parts of the section. To achieve this goal without previous failure by instability of thin cross section parts, the limit ratio of depth to thickness recommended in EC4 (2005) is observed for bending and compression. As demonstrated by Han *et al.* (2010), CFDST columns exhibits three failure modes as inner tube failure, outer tube failure and both tubes failure. To achieve the best performance, the columns must be designed in such a way as to make yielding or buckling of outer tube as the dominant mode of failure. In addition, buckling of inner tube may result in a loss of confining pressure on in-filled concrete. Therefore, the required minimal thickness of inner tube to prevent its premature yielding and buckling failure can be calculated by the following equation (Han *et al.* 2010)

$$t \geq \begin{cases} \frac{D_i f_{yo} t_o}{f_{yi}} \\ \sqrt{\frac{6 D_i^2 f_{yo} t_o}{2.27 D E}} \end{cases} \quad (1)$$

where f_{yo} and f_{yi} are yield stress of the outer tube and inner tube, respectively, t_o = thickness of the outer tube, D_i = diameter of the inner tube and D = diameter of confined

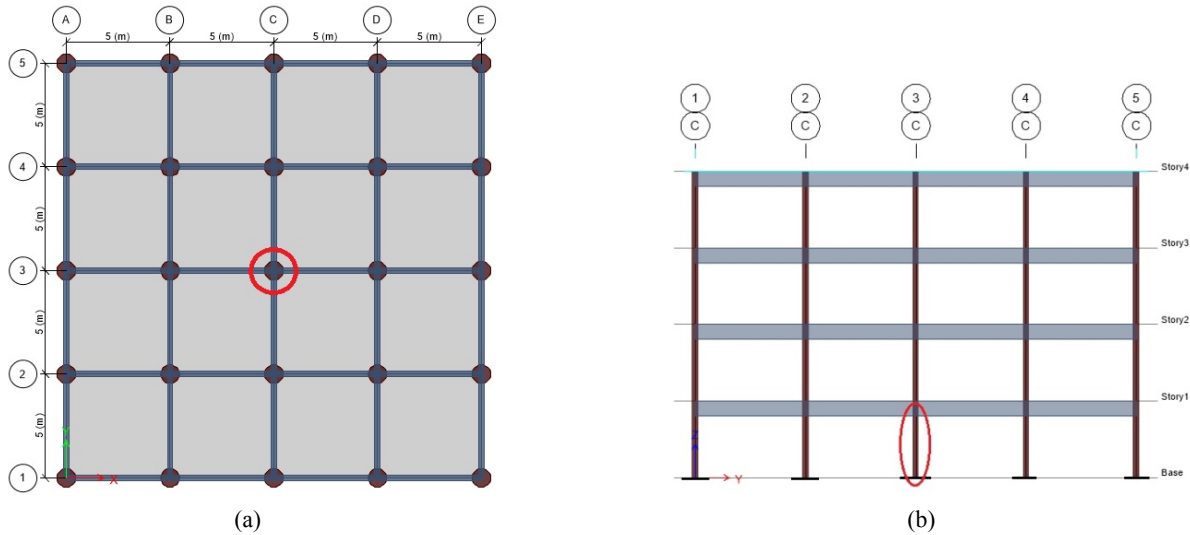


Fig. 1 Considered CFDST column; (a) Typical floor plan; (b) Elevation

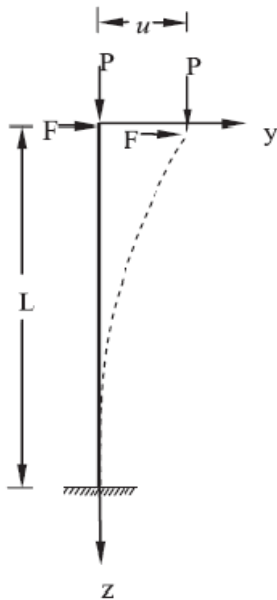


Fig. 2 Axial and lateral loads applied at top of CFDST column

concrete.

Assuming a steel yield strength of 344 MPa (obtained from coupon tests (Imani *et al.* 2015)) and taking $D_i = 150$ mm and $D_o = 300$ mm for the outer tube and the inner tube diameters, respectively, and assuming outer tube thickness equal to 4 mm, Eq. (1) gives $t = 2.0$ mm. The selected geometrical magnitudes are practical sizes for low-rise building columns.

The minimum thickness of the outer tube is selected based on the EC4 to meet the local buckling prevention requirement

$$\frac{D}{t} = 90 \sqrt{\frac{235}{f_{yo}}} \quad (2)$$

Slenderness and section compactness for concrete filled

tubes, per the AISC Specification (AISC 2010a, b), is controlled. For circular outer tube, the section slenderness ratio is 75 complying with the non-compactness limits $0.09E/f_{yo} < D/t < 0.31E/f_{yo}$. The story height is presumed to be 3.5 m.

The numerical plan includes 24 circular CFDST columns with longitudinal stiffeners and transverse stiffeners and as well as a reference ordinary CFDST column without any stiffeners. The models can be divided into three groups: (i) columns stiffened by longitudinal stiffeners employed on the inner or outer tube; (ii) columns stiffened by external rings welded on the outer tube; (iii) reference column. The schematic representation of these models is illustrated in Fig. 3. Longitudinal stiffening scheme is achieved by adding four or six longitudinal stiffeners on the exterior or interior surfaces of the outer or inner tubes. It should be noted that the stiffeners are placed symmetrically on the inner or outer tube. In different cases of embedding longitudinal stiffeners on the inner or outer tubes, two cases involving same cross section area and same moment of inertia are considered separately. External rings serving as transverse stiffeners are welded to the outer tube. Details of CFDST columns are provided in Table 1, where model designations starting with a “C” refers to model with the outer circular tube. The second letter “C” stands for the inner circular tube. The letters “IO”, “EO” and “EP” represents the position of the longitudinal stiffeners in the “interior surface of outer tube”, “exterior surface of outer tube” and “exterior surface of inner tube”, respectively. In order to designate the specimens with longitudinal and transverse stiffeners, an additional character “L” and “T” is used to label them, respectively. The numeral in the labels indicates the number of longitudinal or transverse stiffeners. The last character “A” and “M” implies the same cross-section area and the same moment of inertia, respectively. The wall thickness of rings is 10 mm. Total cross section of the stiffeners is taken 1400 mm² in the stiffened models involving the same cross section area. However, the column moment of inertia is assumed to be 386.749 mm⁴ in the models with the same moment of inertia.

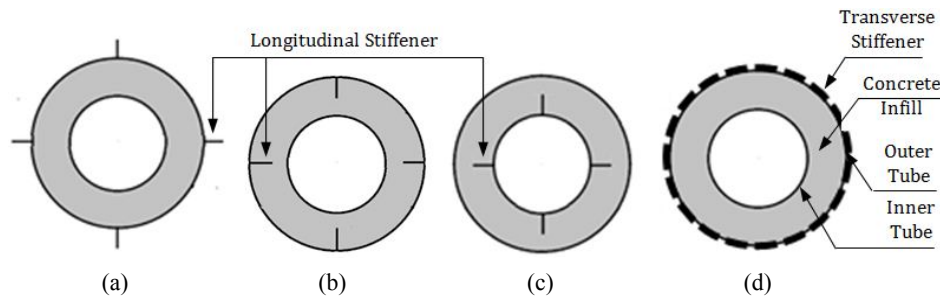


Fig. 3 Stiffening schemes of CFDST column: (a) CC-EO; (b) CC-IO; (c) CC-EI; (d) CC-EO-T

Table 1 Summary of the studied CFDST specimens

No.	Model label	Outer tube	Inner tube	Stiffeners	n	Load	f_{cu}	f_y	End cond.
		$D_o \times t_o$	$D_i \times t_i$						
		(mm×mm)	(mm×mm)	(mm×mm)	(kN)		(Mpa)	(Mpa)	
1	CC	300 × 4	150 × 2	—	0.4	1072.06	55	344	Fixed-Free
2	CC-EO-L-4-A	300 × 4	150 × 2	4(35 × 10)	0.4	1254.33	55	344	Fixed-Free
3	CC-IO-L-4-A	300 × 4	150 × 2	4(35 × 10)	0.4	1214.02	55	344	Fixed-Free
4	CC-EI-L-4-A	300 × 4	150 × 2	4(35 × 10)	0.4	1183.43	55	344	Fixed-Free
5	CC-EO-L-6-A	300 × 4	150 × 2	6(35 × 6.6667)	0.4	1254.10	55	344	Fixed-Free
6	CC-EO-L-4-M	300 × 4	150 × 2	4(25 × 8.793)	0.4	1184.07	55	344	Fixed-Free
7	CC-IO-L-4-M	300 × 4	150 × 2	4(35 × 10)	0.4	1214.02	55	344	Fixed-Free
8	CC-EI-L-4-M	300 × 4	150 × 2	4(40 × 15.845)	0.4	1276.77	55	344	Fixed-Free
9	CC-EO-L-6-M	300 × 4	150 × 2	6(28 × 5.14)	0.4	1183.18	55	344	Fixed-Free
10	CC-EO-T-19	300 × 4	150 × 2	19 ϕ 20	0.4	1072.06	55	344	Fixed-Free
11	CC-EO-T-10	300 × 4	150 × 2	10 ϕ 20	0.4	1072.06	55	344	Fixed-Free
12	CC-EO-T-4	300 × 4	150 × 2	4 ϕ 20	0.4	1072.06	55	344	Fixed-Free
13	CC-EO-T-14	300 × 4	150 × 2	14 ϕ 20	0.4	1072.06	55	344	Fixed-Free
14	CC	300 × 4	150 × 2	4(35 × 10)	0.4	1545.53	55	344	Fixed-Guided
15	CC-EI-L-4-A	300 × 4	150 × 2	4(35 × 10)	0.4	1713.56	55	344	Fixed-Guided
16	CC-EO-L-4-A	300 × 4	150 × 2	4(35 × 10)	0.4	1738.67	55	344	Fixed-Guided
17	CC-EO-L-6-A	300 × 4	150 × 2	6(35 × 6.6667)	0.3	904.602	55	344	Fixed-Free
18	CC-EO-L-6-A	300 × 4	150 × 2	6(35 × 6.6667)	0.5	1567.67	55	344	Fixed-Free
19	CC-EO-L-6-A	300 × 4	150 × 2	6(35 × 6.6667)	0.6	1881.2	55	344	Fixed-Free
20	CC-EO-L-6-A	300 × 4	73 × 1	6(35 × 6.6667)	0.4	1308.2	55	344	Fixed-Free
21	CC-EO-L-6-A	300 × 4	219 × 3	6(35 × 6.6667)	0.4	1132.35	55	344	Fixed-Free
22	CC-EO-L-6-A	300 × 4	150 × 2	6(35 × 6.6667)	0.4	1065.27	35	344	Fixed-Free
23	CC-EO-L-6-A	300 × 4	150 × 2	6(35 × 6.6667)	0.4	1424.24	75	344	Fixed-Free
24	CC-EO-L-6-A	300 × 4	152 × 2	6(35 × 6.6667)	0.4	1578.48	95	344	Fixed-Free

Axial load level (n), the ratio of load on the columns to ultimate capacity of the columns is 0.4, except where specially indicated. In determining the load bearing capacity of the stiffened CFDST columns, the formulations recommended in AISC-360-10 specification (AISC 2010a) are adopted. The models are also subjected to a quasi-static cyclic loading, which began with very small values of the overall drift and increased gradually until drift of 7.88% in accordance with the ATC-24 test protocol (1992). In Fig. 4, the load protocol applied on all the specimens is shown.

In determining the load bearing capacity of the stiffened

CFDST columns, the formulations recommended in AISC-360-10 specification (AISC 2010a) is modified as follow considering the effect of stiffeners

$$P_n = \begin{cases} P_o [0.658^{(P_o/P_e)}] & \text{if } P_e \geq 0.44P_o \\ 0.877P_e & \text{if } P_e < 0.44P_o \end{cases} \quad (3)$$

where

$$P_o = A_s f_y + 0.95 A_c f'_{cc}; \quad P_e = \frac{\pi^2}{(KL)^2} (E_s I_s + C_3 E_c I_c);$$

$$E_C = 0.043W_C^{1.5}\sqrt{f_{CC}}MPa; \quad C_3 = 0.6 + \frac{2A_S}{A_S + A_C} \leq 0.9$$

In the above equations, A_S and A_C are the cross-section areas of structural steel (including inner and outer tubes as well as stiffeners) and concrete, respectively. Also, I_S and I_C are the moments of inertia of steel components and concrete, respectively. In addition, f_{CC} , E_C , E_S and W_C are the confined compressive strength of concrete, the modulus of elasticity of concrete, the modulus of elasticity of steel and the density of concrete, respectively. The constant K is the effective length factor.

In the analysis, the loads are applied in two stages to account for both gravity and lateral loads. The gravity load, $0.4P_u$ (P_u represent the ultimate load of each specimen), is applied as a ramp loading function, and maintained constant once it has reached the peak gravity load level. The lateral load as shown in Fig. 2, is applied at the top of the column in a cyclic manner according to the guidelines proposed by an ATC-24 (1992). The target displacement adopted in this study corresponds to at least 20% strength degradation per FEMA P695 (2009). It is worth noting that assuming a constant load ratio facilitates a comparison of the performance characteristics of the stiffened models.

To evaluate the structural response of the models undergoing large inelastic deformations, two types of ductility, namely displacement ductility and energy-based ductility are used. The displacement ductility is expressed as

$$\mu_D = \frac{\Delta_u}{\Delta_y} \tag{4}$$

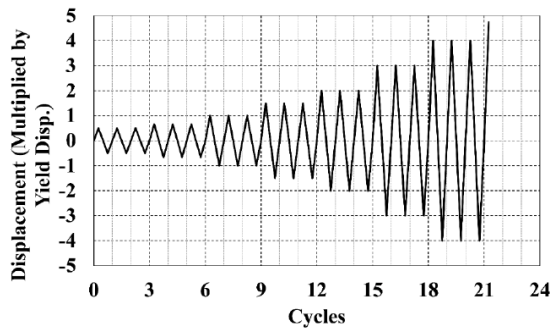


Fig. 4 Cyclic displacement control protocol (ATC 1992)

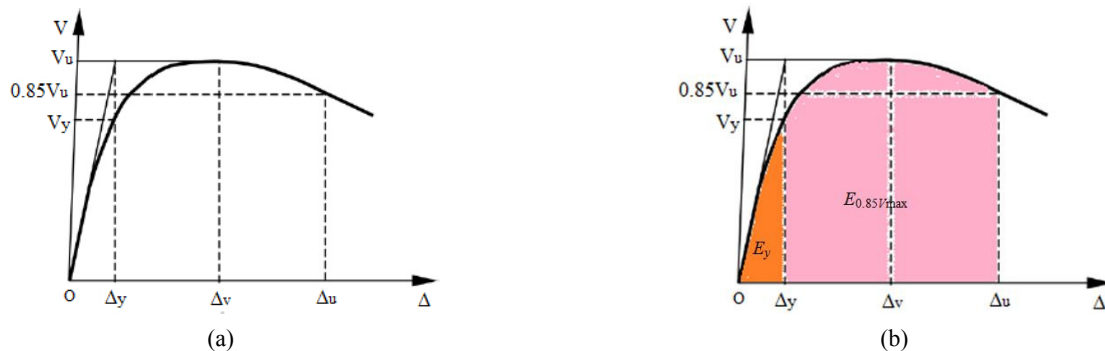


Fig. 5 Envelope of cyclic lateral load (V) versus lateral deflection (Δ) response; (a) determining displacement-based ductility (Han *et al.* 2006); (b) determining energy-based ductility (Duarte *et al.* 2016)

where Δ_y is the yielding displacement and Δ_u is the displacement at the point of 15% strength loss ($0.85V_{max}$), as shown in Fig. 5(a).

The energy-based ductility factor μ_E is computed by means of

$$\mu_E = \frac{E_{0.85V_{max}}}{E_y} \tag{5}$$

where $E_{0.85V_{max}}$ is the dissipated energy at the location of $0.85V_{max}$ in the post-peak zone of the envelope curves and E_y is the elastic energy at the onset of first-yielding of the columns. The energy is obtained by computing the area below the load-displacement envelope curve. The values of $E_{0.85V_{max}}$ and E_y are calculated at the referred points, as illustrated in Fig. 5(b) by the shaded areas.

2.2 Finite element mesh of the models

A FE model is developed for each of the CFDST columns with the aid of ABAQUS software. These models are used to capture the results including the hysteretic loading–displacement curves, cumulative dissipated energies, ductility ratios as well as the local and global deformations. The models include outer tube, inner tube, plain concrete core and stiffeners.

All the parts are modeled with C3D6R element, which refers to a three dimensional 6-node, solid element with reduced integration and large-strain formulation. However, the C3D8R solid elements are used to mesh the concrete infill and steel tubes in structural analyses of the unstiffened CFDST columns. The reason for using six node solid elements instead of eight node ones in the stiffened CFDST columns is to provide adequate surfaces to benefit the interaction between concrete and stiffeners.

The interaction between the steel tubes (or stiffeners) and the concrete core of CFDST columns affects the overall behavior of these columns. Therefore, the development of a model to accurately simulate this interaction is one of the most challenging parts of the modeling process. A three dimensional surface-to-surface type contact pair is assigned to the connection between steel and concrete core. In this respect, the concrete surface around steel is considered as the master surface and steel itself is the slave surface. The “hard contact” is selected to represent the normal behavior of concrete-tubes and concrete-stiffeners interactions. When

a contact pair is in contact, there is pressure between the master and slave surfaces, whereas two contact surfaces separate as the pressure comes to zero. The ‘penalty’ friction is used to simulate the tangential behavior of the concrete-tubes and concrete-stiffeners interactions with a coefficient of friction equal to 0.25. Values of 0.20 to 0.3 have been typically used and proven to provide satisfactory results compared to experiments (Johansson and Gylltoft 2001, Espinos *et al.* 2010). When the shear stress in the interface is smaller than a certain value, no slipping occurs, otherwise slipping occurs between surfaces. The stiffeners are tied to the steel tube.

Using of more elements in the model may enhance the effectiveness of hourglass stiffness in restricting the hourglass modes. Therefore, refined mesh may lead to acceptable results when linear reduced integration elements are used in the model. The mesh-size used is optimized with respect to the preliminary works, considering computational capacity, running-time and the robustness of the results. Suitable mesh pattern is feasible on identifying the parts of columns subjected to large inelastic deformation and local buckling and using a finer mesh at those locations. Mesh dimensions of approximately 10×10 mm and 25×25 mm are used for bottom end and remaining part of CFDST columns, respectively, prove to be sufficient to predict with enough accuracy the mechanical behavior of these columns under cyclic loading. The general view and a close-up of the FE model are illustrated in Fig. 6.

2.3 Material modeling of steel

The elasto-plastic model is used for the steel material in the analysis. The Young’s modulus E_s is set to be 200 GPa, while the Poisson’s ratio ν is set to be 0.3. The yield stress of 344 MPa, the tensile strength of 400 MPa and the fracture strain of 0.2, obtained from coupon tests on the outer tube (Imani *et al.* 2015), are assumed for both steel tubes as well as stiffeners.

The plastic property of steel is defined by means of the defined true stress, true strain relation. Combined hardening – which considers both isotropic and kinematic hardenings

– is selected to represent hardening behavior. The Von Mises plasticity with a general three dimensional stress state is employed which implies the yield condition at step $m+1$ as (Kojic and Bathe 2005)

$${}^{m+1}f_y = \frac{1}{2} {}^{m+1}S \cdot {}^{m+1}S - \frac{1}{3} {}^{m+1}\sigma_y^2 = 0 \quad (6)$$

where ${}^{m+1}\sigma_y$ is the yield stress at step $m+1$ and ${}^{m+1}S$ is the deviatoric stress tensor with the components (Kojic and Bathe 2005)

$${}^{m+1}S_{ij} = \sigma_{ij} - \sigma_{ave} \delta_{ij} \quad (7)$$

$\sigma_{ave} = \sigma_{ij} / 3$ is the mean stress. The FE model does not address low-cyclic fatigue and fracture.

2.4 Material modeling of concrete

Crushing and cracking of the concrete, especially in buckled areas, seem inevitable in CFDST columns. Therefore, it is necessary to select appropriate material models in order to represent the nonlinear behavior of concrete part. In the elastic range the elastic modulus and the Poisson’s ratio are specified. The Poisson’s ratio of concrete is taken as 0.2. The elastic modulus of concrete E_c correlated to its compressive strength and is given by ACI 318-11 (ACI 2008) as

$$E_c = 4700 \sqrt{f'_{cc}} \quad (8)$$

where f'_{cc} is the confined strength of concrete in MPa.

Among the modeling features of ABAQUS, the Concrete Damage Plasticity model is used to implement the non-linear behavior of the concrete. This option considers two main failure mechanisms, namely tensile cracking and compression crushing for this material (ABAQUS 2012).

In CFDST columns, the outer and inner tubes confine the in-filled concrete. A schematic representation of stress–strain curve of the confined concrete, as well as that of the unconfined concrete is given in Fig. 7. The uniaxial compressive stress– strain formulae developed by Hu and

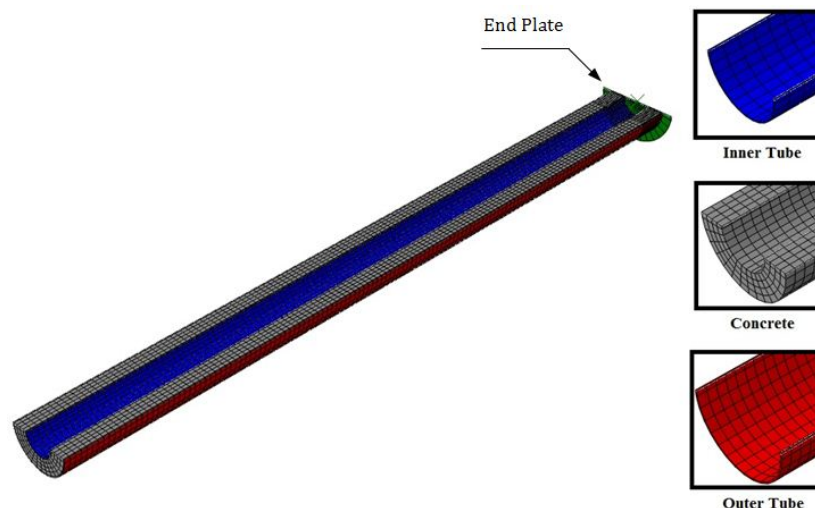


Fig. 6 Three-dimensional finite element model for CFDST columns

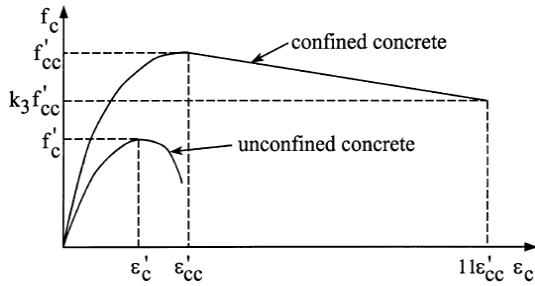


Fig. 7 Stress–strain curves for both confined and unconfined concrete (Pagoulatou *et al.* 2014)

Su (2011) and Pagoulatou *et al.* (2014) based on the Mander *et al.* (1988) suggestion is adopted for the sandwiched concrete which takes confinement effects into account by both mechanical and geometrical properties of inner and outer steel tubes. The confined compressive strength f'_{cc} and corresponding strain ϵ'_{cc} are estimated by the following equations

$$f'_{cc} = f'_c + k_1 f_l \quad (9)$$

$$\epsilon'_{cc} = \epsilon'_c \left(1 + k_2 \frac{f_l}{f'_c} \right) \quad (10)$$

where the coefficients k_1 and k_2 are constants and should be set to 4.1 and 20.5, respectively as recommended in the study of Richart *et al.* (1928). The term f'_c stands for the unconfined cylinder strength of concrete, whereas ϵ'_c represents the corresponding unconfined strain. Additionally, f_l represents the confining pressure around the concrete core considering the influence of both tubes which is obtained from the following three equations

$$f_l = 8.525 - 0.166 \left(\frac{D_o}{t_o} \right) - 0.00897 \left(\frac{D_i}{t_i} \right) + 0.00125 \left(\frac{D_o}{t_o} \right)^2 + 0.00246 \left(\frac{D_o}{t_o} \right) \left(\frac{D_i}{t_i} \right) - 0.00550 \left(\frac{D_i}{t_i} \right)^2 \geq 0 \quad (11)$$

$$\frac{f_l}{f_{yt}} = 0.01844 - 0.00055 \left(\frac{D_o}{t_o} \right) - 0.00040 \left(\frac{D_i}{t_i} \right) + 0.00001 \left(\frac{D_o}{t_o} \right)^2 + 0.00001 \left(\frac{D_o}{t_o} \right) \left(\frac{D_i}{t_i} \right) - 0.00002 \left(\frac{D_i}{t_i} \right)^2 \quad (12)$$

$$\frac{f_l}{f_{yo}} = 0.01791 - 0.00036 \left(\frac{D_o}{t_o} \right) - 0.00013 \left(\frac{D_i}{t_i} \right) + 0.00001 \left(\frac{D_o}{t_o} \right)^2 + 0.00001 \left(\frac{D_o}{t_o} \right) \left(\frac{D_i}{t_i} \right) - 0.00002 \left(\frac{D_i}{t_i} \right)^2 \quad (13)$$

where, D_o and t_i are the diameter of the outer and thickness of inner tube, respectively.

It is worth noting that the use of such constitutive relation that is capable of describing these effects is essential, since the dilatancy of concrete is opposed by ties which thus produce hydrostatic pressure in concrete thereby increasing its ductility. To predict the nonlinear behavior of

concrete up to f'_{cc} , the following equation, proposed by Saenz (1964) is employed

$$f_c = \frac{E_c \epsilon'_c}{1 + (R + R_E - 2(\epsilon / \epsilon'_{cc})) + (2R - 1)(\epsilon / \epsilon'_{cc})^2 + R(\epsilon / \epsilon'_{cc})^3} \quad (14)$$

where R_E and R are obtained using the following equations

$$R_E = \frac{E_c \epsilon'_{cc}}{f'_c} \quad (15)$$

$$R = \frac{R_E}{3} - \frac{1}{R_E} \quad (16)$$

To simulate the tensile behavior of plain concrete, the concept of fracture energy is a better solution. The fracture energy is defined as the energy required to open unit area of crack surface (ABAQUS 2012). The fracture energy (G_f) proposed by Lu *et al.* (2011) is used in the analysis which can be expressed by the following equation

$$G_f = \alpha \times \left(\frac{f'_c}{10} \right)^{0.7} \times 2.5 \times 10^{-3} \quad (17)$$

$$\alpha = 1.25 d_{\max} + 10$$

where, d_{\max} is the maximum diameter of coarse aggregate in millimeter.

Other parameters required for the concrete damage plasticity model, including the ratio of the compressive strength under biaxial loading to uniaxial compressive strength (f_{bo}/f_c), dilation angle (ψ), and the ratio of the second stress invariant on the tensile meridian to that on the compressive meridian (K_c), are evaluated according to the suggestions of Tao *et al.* (2013)

$$\psi = 10^\circ \quad \frac{f_{bo}}{f_c} = \frac{1.5}{f_{cc}^{0.075}} \quad (18)$$

$$K_c = \frac{5.5}{5 + f_{cc}^{0.075}} \quad (19)$$

The compressive stress–strain behavior of concrete core, used for structural analyses, is shown in Fig. 8(a).

For tension behavior of concrete, the tensile strength of that, f'_t , is assumed to be $f'_t = 0.1 f'_{cc}$. It has been shown in the literature; the concrete damage plasticity model due to assumption of isotropic plasticity in tension is considerably approximate in terms of the tensile behavior and cannot simulate tensile cracking of the in-filled concrete, realistically. Crack opening and crack closing produced typical pinching of the hysteresis curves during load excursions on concrete filled columns (Goto *et al.* 2010, Imani *et al.* 2014). One approach to resolve this issue concerned with the concrete damage plasticity model is to use discrete crack model at the location of the observed major horizontal tensile crack (Goto *et al.* 2010). A cohesive interaction is modeled between the two surfaces of the discrete crack to be able to simulate its opening and closing behavior. It is worth noting that when the tensile

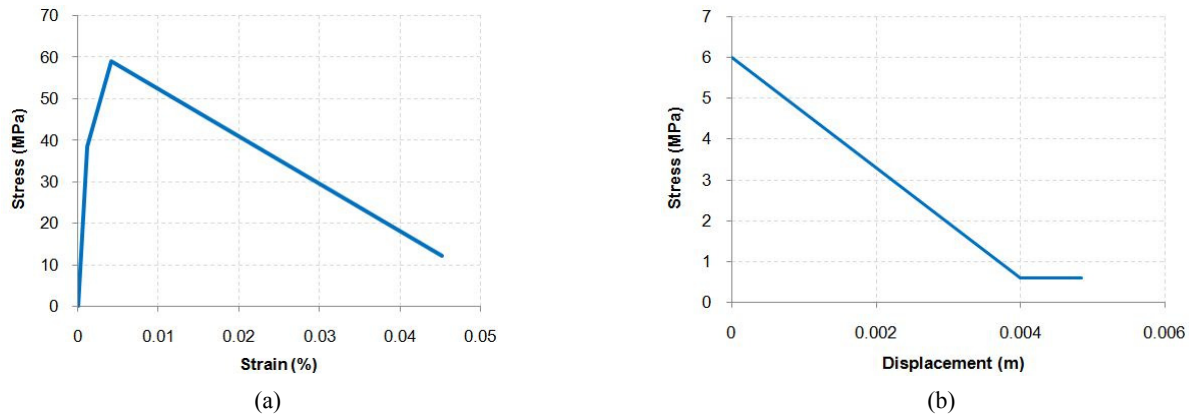


Fig. 8 (a) Compressive stress-strain relationship for concrete core; (b) Tensile stress–displacement relationship used for modeling concrete

crack happens, the tensile stress-strain relation no longer accurately represent the material's behavior. A viable alternative is to use stress-displacement curve to represent the softening response after crack initiation which decreases the mesh-dependency of the results (ABAQUS 2012). Fig. 8(b) shows the stress-displacement curve used in the FE model.

2.5 Imperfection

The construction process inevitably induces some imperfections on comprising elements of the fabricated sections. The imperfection in the straightness of the columns is of particular concern. The initial straightness imperfection is converted into load initial eccentricity at the ends of the columns. Therefore, the initial geometric imperfection of the studied CFDST columns is simulated by load eccentricity. The value of $L/1000$ employed by the majority of researchers is taken as load eccentricity (Tao *et al.* 2013).

2.6 Verification of the FE model

The verification of the developed FE model is achieved

via comparison with the experimental data. To this end, two CFDST columns (S1 and S2) tested under cyclic loading at the Univ. at Buffalo by Imani *et al.* (2014) and eight CFDST beam-column specimens with CHS outer and CHS inner (CC2-1, CC2-2, CC2-3, CC2-4, CC3-1, CC3-2, CC3-3 and CC3-4) subjected to cyclic bending tested by Han *et al.* (2006) are considered for validation. Dimensions, loading protocol and material properties are the same as experimental conditions. Table 2 gives the geometric and material properties of the specimens. Fig. 9 shows the finite element mesh for the CFDST specimens tested. The S1 specimen was subjected to cyclic displacements until the onset of inelastic local buckling, while the S2 specimen was pushed further with additional cycles up to developing more severe local buckling.

A comparison between experimental and the FE results representing hysteresis curves of the lateral load versus lateral displacement is shown for all the specimens in Fig. 10. There is good agreement between experimental and the current numerical hysteresis plots. However, the discrepancies between numerical and experimental results are deemed acceptable, and understand to be a consequence of experimental uncertainties and modeling assumptions.

Table 2 Geometrical and mechanical properties of experimental specimens (verified models)

Specimen	Axial load (kN)	Outer tube	Inner tube	f_y (Mpa)		f_u (Mpa)		f_c (MPa)	End condition	L (mm)
		$D_o \times t_o$ (mm×mm)	$D_i \times t_i$ (mm×mm)	Inner tube	Outer tube	Inner tube	Outer tube			
S1	316	203.2 × 2.79	127 × 2.29	303	344	365	400	55.8	Fixed-Free	2705
S2	356	203.2 × 2.79	127 × 2.29	303	344	365	400	60	Fixed-Free	2705
CC2-1	0	114 × 3	32 × 3	422.3	308	-	-	32	Pined-Pined*	1500
CC2-2	153	114 × 3	32 × 3	422.3	308	-	-	32	Pined-Pined*	1500
CC2-3	306	114 × 3	32 × 3	422.3	308	-	-	32	Pined-Pined*	1500
CC2-4	459	114 × 3	32 × 3	422.3	308	-	-	32	Pined-Pined*	1500
CC3-1	0	114 × 3	58 × 3	374.5	308	-	-	32	Pined-Pined*	1500
CC3-2	144	114 × 3	58 × 3	374.5	308	-	-	32	Pined-Pined*	1500
CC3-3	288	114 × 3	58 × 3	374.5	308	-	-	32	Pined-Pined*	1500
CC3-4	432	114 × 3	58 × 3	374.5	308	-	-	32	Pined-Pined*	1500

*Free axial displacement at one end is allowed as in the test setup

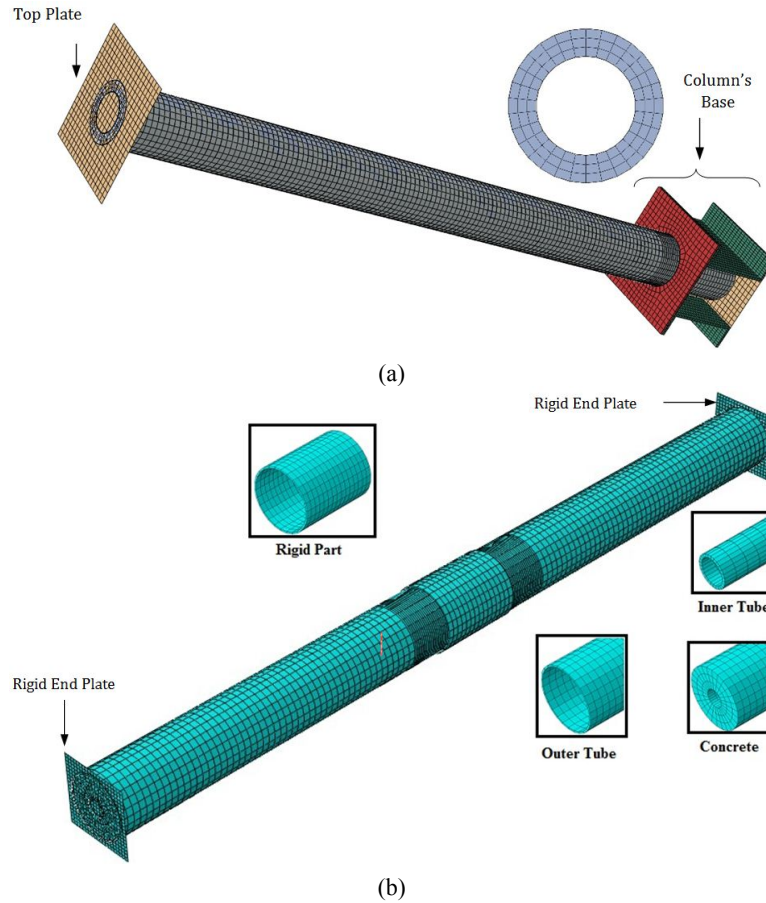


Fig. 9 Finite element mesh for the verified CFDST models: (a) S1 and S2 specimens; (b) CC2-1 ~ CC3-4 specimens

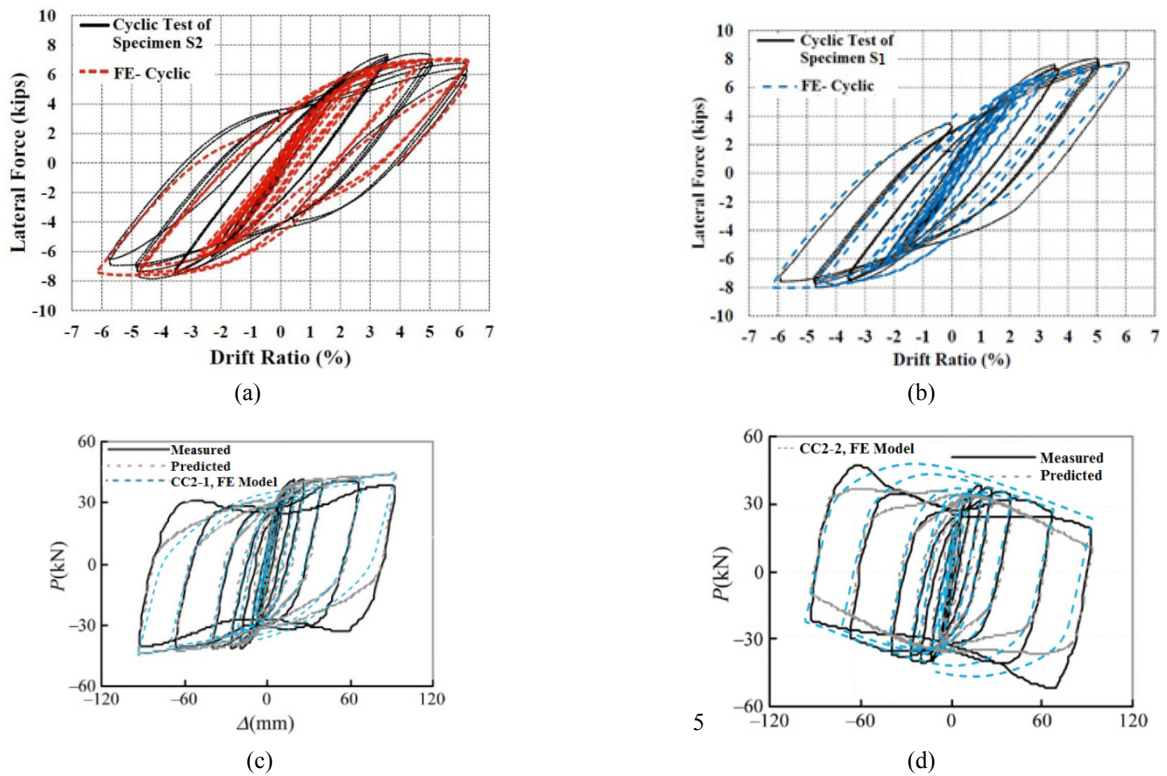


Fig. 10 Comparison between experimental and numerical hysteretic curve of the verified models: (a) specimen S1; (b) specimen S2; (c) specimen CC2-1; (d) specimen CC2-2; (e) specimen CC2-3; (f) specimen CC2-4; (g) CC3-1; (h) CC3-2; (i) CC3-3; (j) CC3-4

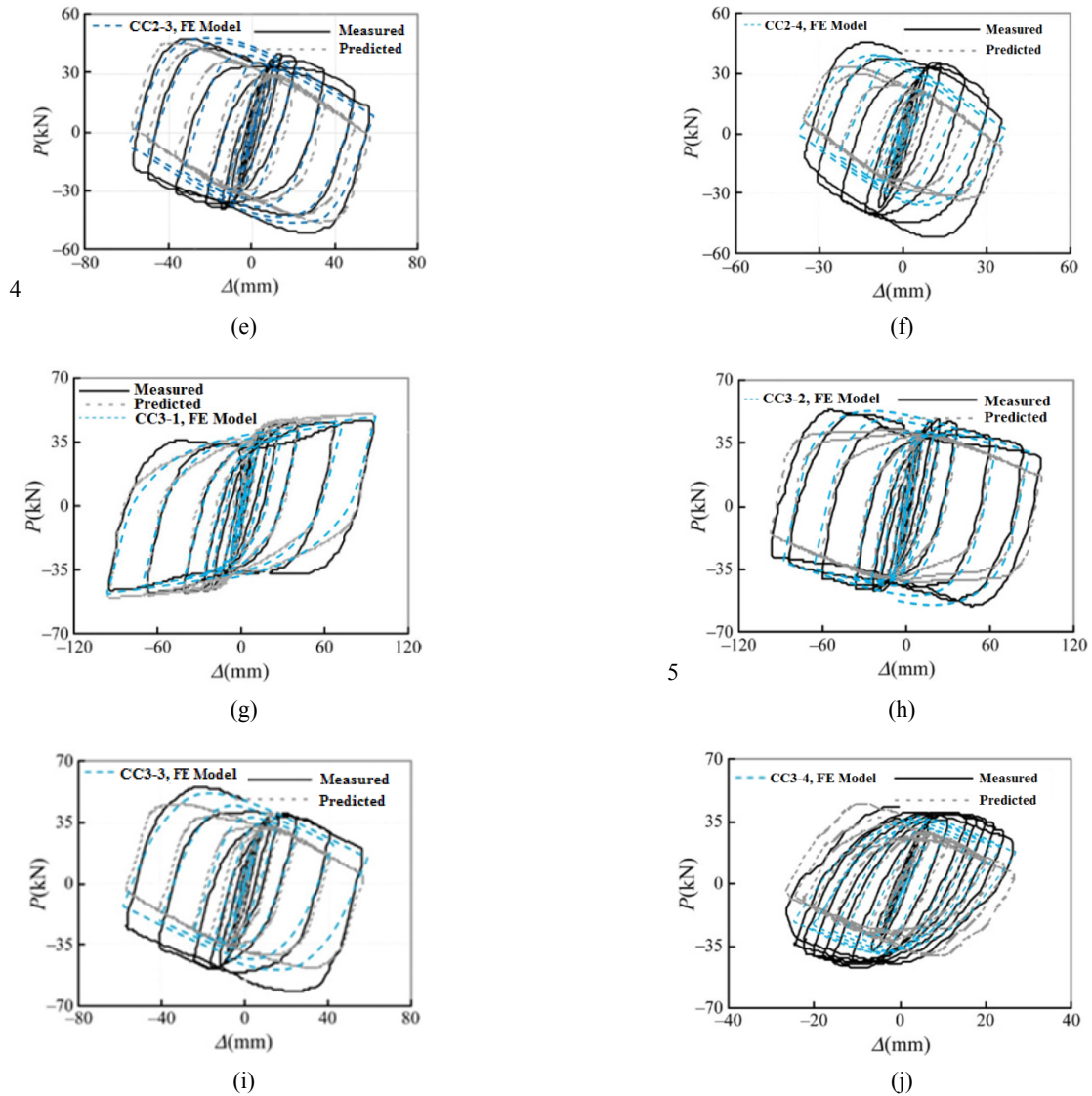


Fig. 10 Continued

The hysteresis loops of CC2-1 ~ CC3-4 beam-column specimens exhibit no clear signs of pinching behavior. However, the pinching of the hysteresis curve in S1 and S2 specimens are captured reasonably well by the FE model.

The maximum lateral strength of 8.00 kips, 7.43 kips, 41.07 kN, 47.0 kN, 47.25 kN, 45.58 kN, 54.08 kN, 54.67 kN, and 40 kN values have been achieved for the

experimental specimens S1, S2, CC2-1, CC2-2, CC2-3, CC2-4 and CC3-1, CC3-2, CC3-3, and CC3-4, respectively. In the numerical models, 7.78 kips, 7.5 kips, 44.7 kN, 47.83 kN, 46.7 kN, 39.43 kN, 49.74 kN, 53.18 kN, 50.94 kN and 38.16 kN are obtained for the maximum lateral strength of the corresponding counterparts, respectively. The resulting differences between predicted and measured strengths are

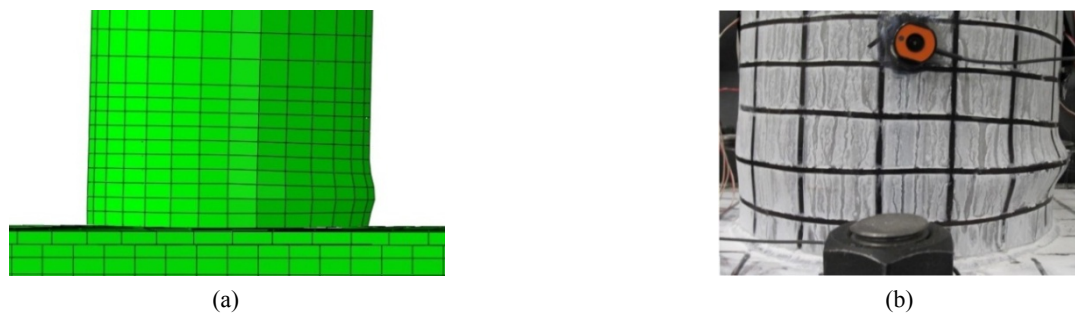


Fig. 11 Comparison between experimental and numerical deformed shapes of specimen S2: (a) Numerical; (b) Experimental

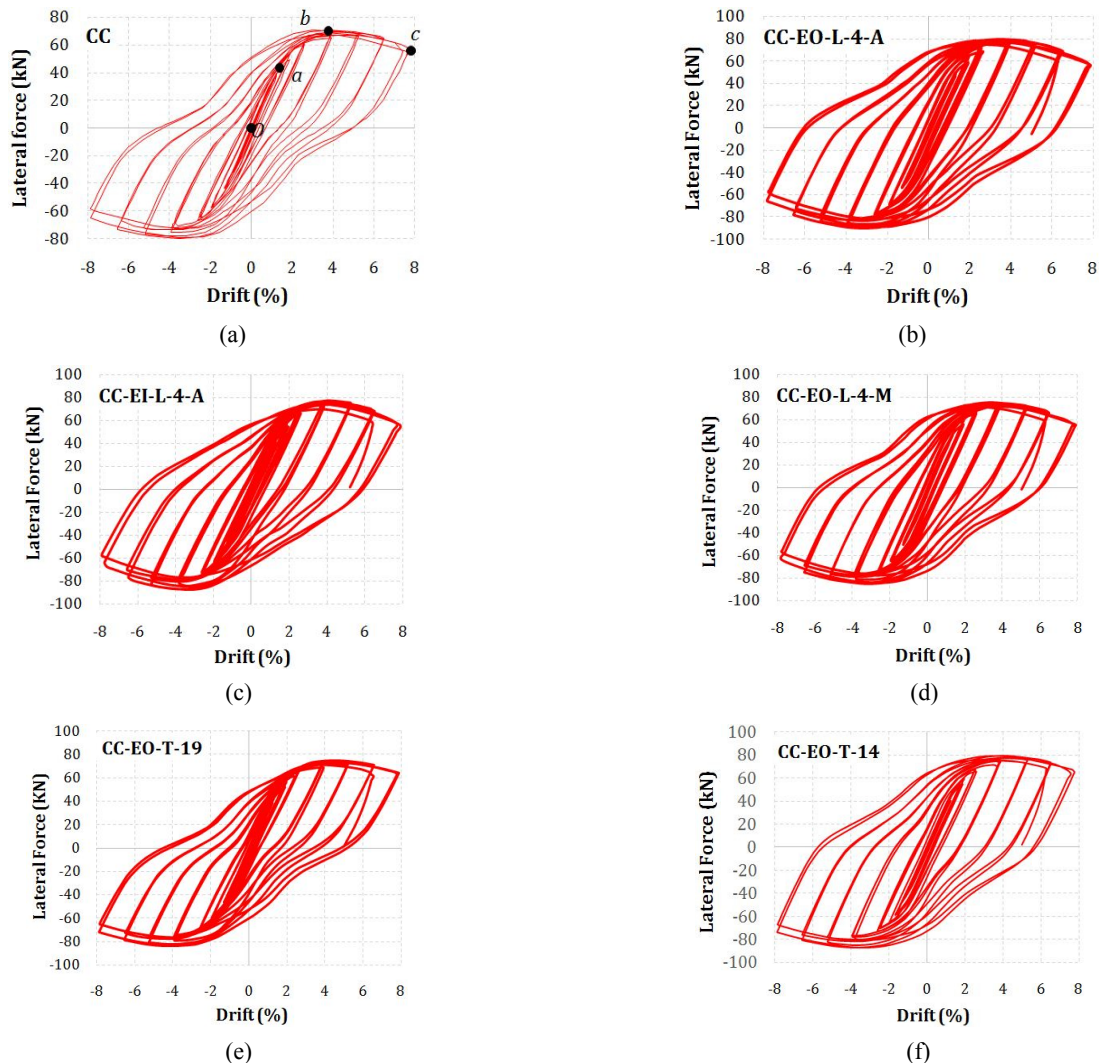


Fig. 12 Force-displacement hysteretic curves: (a) CC; (b) CC-EO-L-4-A; (c) CC-EI-L-4-A; (d) CC-EO-L-4-M; (e) CC-EO-T-19; (f) CC-EO-T-14

small (less than 10%). It can be observed from Fig. 10 that the current FE hysteretic curves are closer to the experimental counterparts more than the numerical curves obtained previously by Han *et al.* (2006) for the tested specimens.

Propagation of the tube buckling and global deformation is comparable to that reported for the experimental specimens. The deformation of the numerical model S2 implying local buckling at the column end consistent with the observations made in the test is illustrated in Fig. 11. It is concluded that the FE model with the discrete concrete crack inserted at the location of major tensile cracks provides sufficiently accurate results and is judged acceptable for the FE analysis simulation of these columns under seismic actions.

3. Analysis results and discussion

3.1 Hysteretic curves and failure modes

The lateral load versus lateral displacement hysteretic

loops with envelope curves for representative CFDST models under cyclic loading are shown in Fig. 12. As can be seen, unloading and reloading in the opposite direction produced typical pinching of the hysteretic curve. The formation of major tensile crack in the inelastic range and its opening and closing in subsequent cycles facilitates the local buckling of the outer tube, resulting in the pinching of the hysteretic curves of these columns. The pinching becomes relatively severe as the deformation increases. From comparison of the shape of loops corresponding to same drift, it can be seen that the maximum strength achieved at first cycles of each displacement degrades as cycling proceeds, mainly due to increased local buckling of the steel tubes and accumulated damage to the sandwiched concrete. By comparing the hysteretic loops of stiffened specimen (e.g., CC-EO-L-4-A) and unstiffened one, CC, it is observed that the pinching behavior is significantly improved with the addition of stiffeners. It is also found that the models with longitudinal stiffeners have plumper loop than the ones with ring stiffeners, especially for the hysteretic loops at their later stage.

The half-cycle of a typical hysteretic curve of CFDST

column (Fig. 12) can be categorized into three classes of behavior:

- (1) From point *o* to point *a*, the models behave in a linear manner. This region does not contribute to the inelastic energy dissipation. The first yielding in the outer tube is found to appear at point *a* under the applied load;
- (2) After point *a*, the model exhibits nonlinear behavior up to point *b* associated with the maximum lateral load. As the non-linearity increases, the plastification progressively spreads over the outer tube accompanied by the inelastic behavior of concrete due to its crushing and cracking;
- (3) From point *b* onward, the lateral load decreases as the lateral displacement increases. This descending branch of envelope curves is due to combined effects of concrete further crushing/cracking, outward local buckling of the outer tube and inward local buckling of the inner tube (Fig. 13).

Table 3 summarizes the plastic drifts of the outer and inner tubes, opening/closing drift of the major concrete tensile crack as well as threshold of local buckling in the

tubes. These columns subjected to cyclic loading are vulnerable to both local and global buckling. The elements will have excessive deformations and, leading to local buckling of the outer and inner tubes at the base of column. This does not necessarily jeopardize the performance characteristics of the column, but rather introduces some local damage at the base of column. The first sign of yielding in the outer tube and the inner tube of CC model, at the end of column, is observed at 1.39% drift and 2.0% drift, respectively. The inelastic local buckling at the base of outer tube as well as closing/opening of concrete crack is initiated at the column end at drift ratio more than 2%. The yielding and buckling of the inner tube is appeared at drift of 2% and 3.9%, respectively. The pronounced local buckling of the outer tube at drift of 5.25% is accompanied by a sudden drop in the lateral load carrying capacity.

In CC-EI-L-4-A and CC-IO-L-4-A models, the interaction effect exerted by the stiffeners on the concrete core leads to performance of the components as a single element. The outer tube plastification and local buckling in CC-IO-L-4-A is appeared at drift of 1.31% and 3.94%, respectively. The inner tube's local buckling is happened at drift of 6.5% which is delayed with respect to that at CC model. This issue is more pronounced in CC-EI-L-4-A column in which no local buckling is observed in the inner

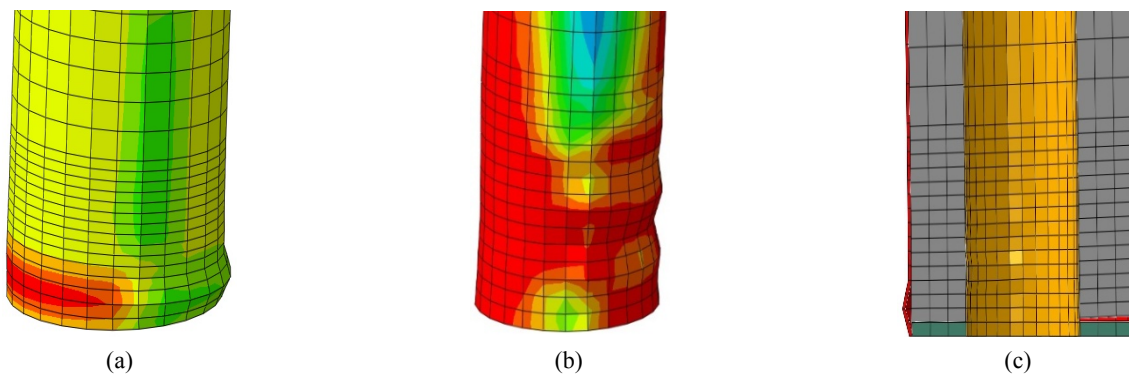


Fig. 13 (a) Outward local buckling of the outer tube; (b) Inward local buckling of the inner tube; (c) Opening/closing the major tensile crack of concrete

Table 3 Drift values corresponding to yielding and local buckling of the outer and inner tube as well as opening/closing of the major concrete tensile crack for the models from the cyclic analysis

Specimen*	Yield drift (%)		Local buckling drift (%)		Opening/Closing	Strength degradation
	Outer tube	Inner tube	Outer tube	Inner tube	Drift (%)	Drift (%)
CC	1.39	2	2	3.9	2	5.25
CC-EO-L-4-A	1.31	2	2.62	3.94	2	3.94
CC-IO-L-4-A	1.39	2	3.94	6.5	2	3.94
CC-EI-L-4-A	1.39	2	2	7.88	2	3.94
CC-EO-L-6-A	1.31	2	2.62	3.94	2	3.94
CC-EO-T-19	1.39	2	2	5.25	2	5.25
CC-EO-T-10	1.39	2	2	5.25	2	5.25
CC-EO-T-4	1.39	2	-	5.25	2	5.25
CC-EO-T-14	1.39	2	-	5.25	2	5.25

* Stiffened CFDST columns including the same moment of inertia have the same trend as the counterparts with the same cross-section area

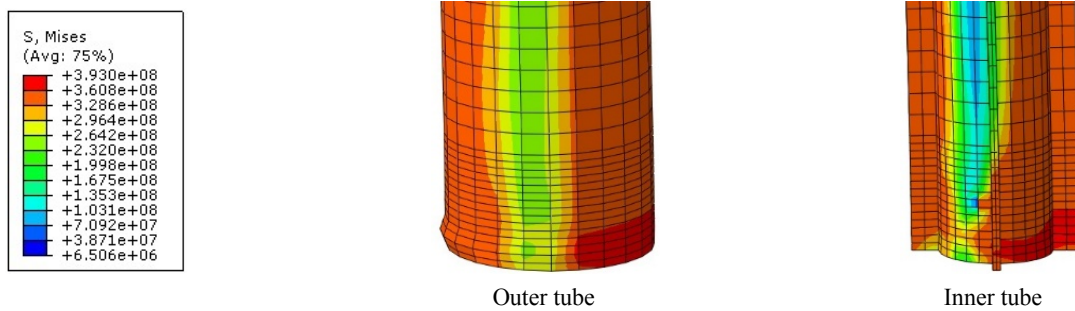


Fig. 14 Von-Mises stress distribution in CC-EI-L-4-A

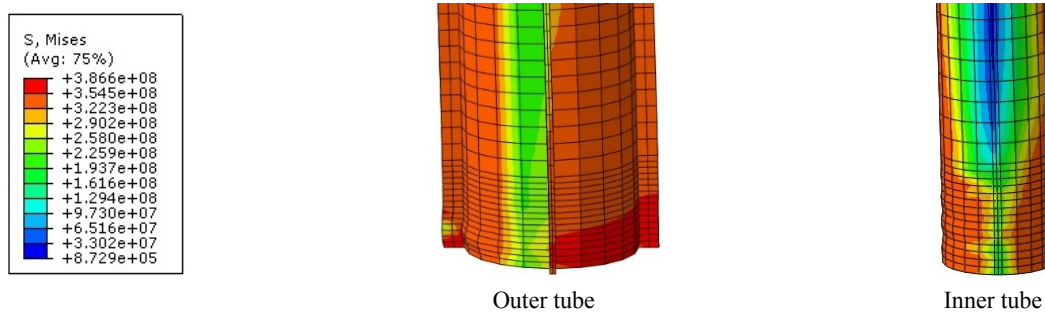


Fig. 15 Von-Mises stress distribution in CC-EO-L-4-A

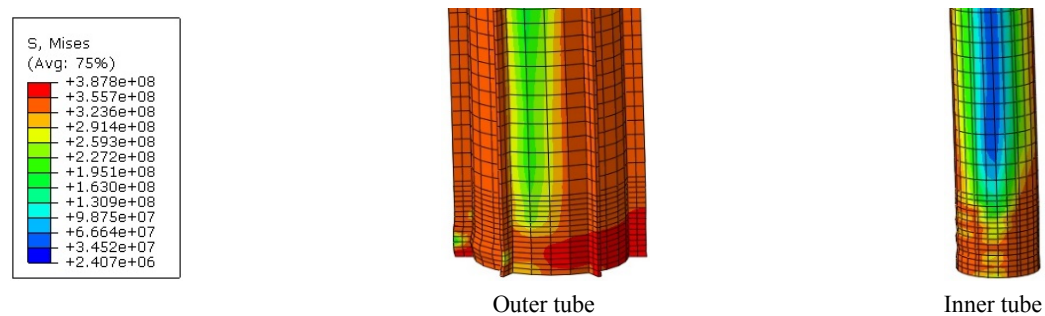


Fig. 16 Von-Mises stress distribution in CC-EO-L-6-A

tube. As can be seen in Fig. 14, the stiffeners are failed due to yielding rather than local buckling. On the contrary, in the CC-EO-L-4-A, the stiffeners in the load path as well as the inner tube experience local buckling (Fig. 15). In the longitudinally stiffened models, local buckling in the outer tube is delayed by adding stiffeners. In addition, the stiffened models exhibit negligible concrete crack opening/closing at drift of 2% compared with the CC model. Therefore, the pinching in these models becomes less severe than in the CC model.

When the stiffeners are sufficiently close (CC-EO-L-6-A), local buckling in the outer tube and inner tube happens at drifts of 2.62% and 3.94%, respectively. Relatively uniform distribution of inelastic Von-Mises stress over the perimeter of CC-EO-L-6-A model than for CC-EO-L-4-A model can be attributed to closer stiffener spacing in the former (Fig. 16). It is observed that the closely spaced stiffeners are effective in preventing local buckling of the outer tube.

In an alternative attempt, using models containing the same moment of inertia with stiffeners is evaluated.

Application of the longitudinal stiffeners with the same moment of inertia in CC-EO-L-4-M, CC-EI-L-4-M and CC-IO-L-4-M models cause the local buckling in the outer tube to be delayed. The shape and changing trend of the hysteretic curves in these models closely parallels that of longitudinally stiffened models with the same cross-section area.

Adding transverse ring stiffeners to stiffen CFDST columns with the aid of increasing confinement pressure provided to the concrete, benefits to steel-concrete interface interaction. In uniform ring-confined CFDST columns, local buckling threshold of the outer tube and inner tube is at drift of 2% and 5.25%, respectively. Such stiffening scheme tends to have a negligible effect on the pinching behavior of the column. As can be seen in Fig. 17, the ring stiffeners that existed at designated positions undergoing minimal stresses cannot prevent the development of the outer tube's local buckling. Preventing local buckling of the outer tube is paramount to precluding premature material fracture and improving performance characteristics of CFDST columns. To delay yielding and local buckling of

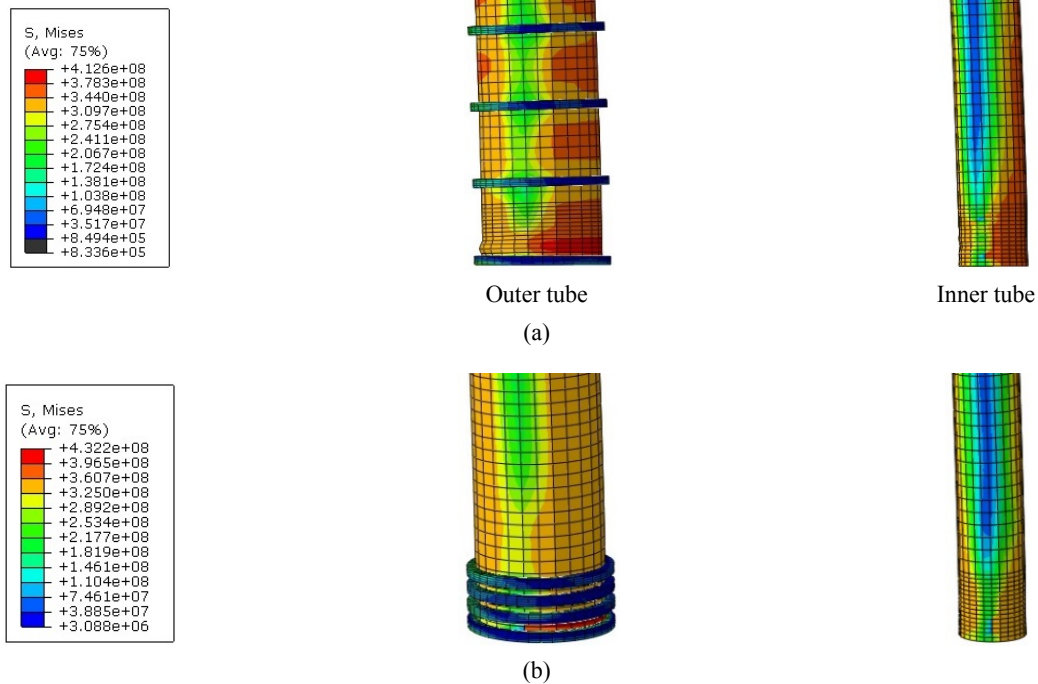


Fig. 17 Von-Mises stress distribution in CC-EO-T: (a) Ring stiffeners along the height of column; (b) Ring stiffeners used at the critical position

the outer tube at the base of these models, ring stiffeners can be only used at this critical location. By doing so, the sandwiched concrete will be subjected to a larger confining pressure and the column behaves more continuously. It is seen that in CC-EO-4-R and CC-EO-14-R, adding ring stiffeners with small spacing at the base of column prevents localized buckling during the cyclic loading process. In addition, the rings added at the base of CFDST columns also restrict the lateral deformation of them at this critical location which led to crushing of the in-filled concrete and inward local buckling of the inner tube at drift of 5.25%. Application of closely spaced ring stiffeners at the base of columns delaying tubes' local buckling improves the pinching behavior of columns.

3.2 Performance characteristics

A comparison of performance characteristics including lateral strength, initial stiffness, energy dissipation, ductility ratio and strength degradation of the stiffened models are presented. The initial stiffness value of each model is calculated by averaging slopes of all the data points over 3 half-cycles. The ability of dissipating the seismic input energy is one of main characteristics of a well-designed lateral resistant structural system; the dissipated energies by the columns are computed in the cycles. The cumulative dissipated energy by the specimens is evaluated from the summation of the areas of loops, obtained from the cyclic loading.

Table 4 shows the maximum lateral load obtained from the cyclic analysis on all the columns. The cyclic loading ended at drift ratio of 7.88% to capture each model's strength degradation. Due to introducing imperfection in the models, the maximum lateral strengths in positive and

negative drifts are not the same. The envelop curves of these models are compared in Fig. 18. It is seen that CFDST columns provided with stiffeners would attain higher strength because the stiffeners contribute at the interaction of steel tubes and concrete surfaces as well as stiffening steel tubes against local buckling. As can be seen in Table 4, the strength of longitudinally stiffened columns is increased by as much as 17%. The stiffeners embedded on the inner tube; result in an increase of strength by 13%. With these stiffeners, considering the constant load level of $n = 0.4$, the stiffened models cannot attain a higher lateral strength at given cyclic loading due to the lower lateral stiffness resulting from the smaller stiffeners' moment of inertia. Among the longitudinally stiffened models with the same cross-section area, the CC-EO-L-6-A and CC-EO-L-4-A models possess the highest amount of shear strength, sequentially.

Results in Fig. 18 show that the models do not lose strength until the 3.94% drift. This issue is due to the fact that until this drift, no outer tube's local buckling develops at the base of columns. Generally, local buckling of the steel tubes and subsequent strength degradation are observed when the cycling loading exceeds 3.94% drift. The strength degradation of the CC model is 16.32%, while the smallest and largest strength degradation in the columns with the same cross section area are 26.4% and 29.57% corresponding to CC-EI-L-4-A and CC-EO-L-4-A, respectively. As shown in Fig. 18, among the stiffening schemes pertaining the same cross section area, the use of longitudinal stiffeners on the outer tube leads to the larger lateral strength and initial stiffness due to the higher lateral stiffness resulting from the larger stiffeners' moment of inertia. All the stiffened CFDST columns with longitudinal steel stiffeners exhibit relatively high initial stiffness (in a

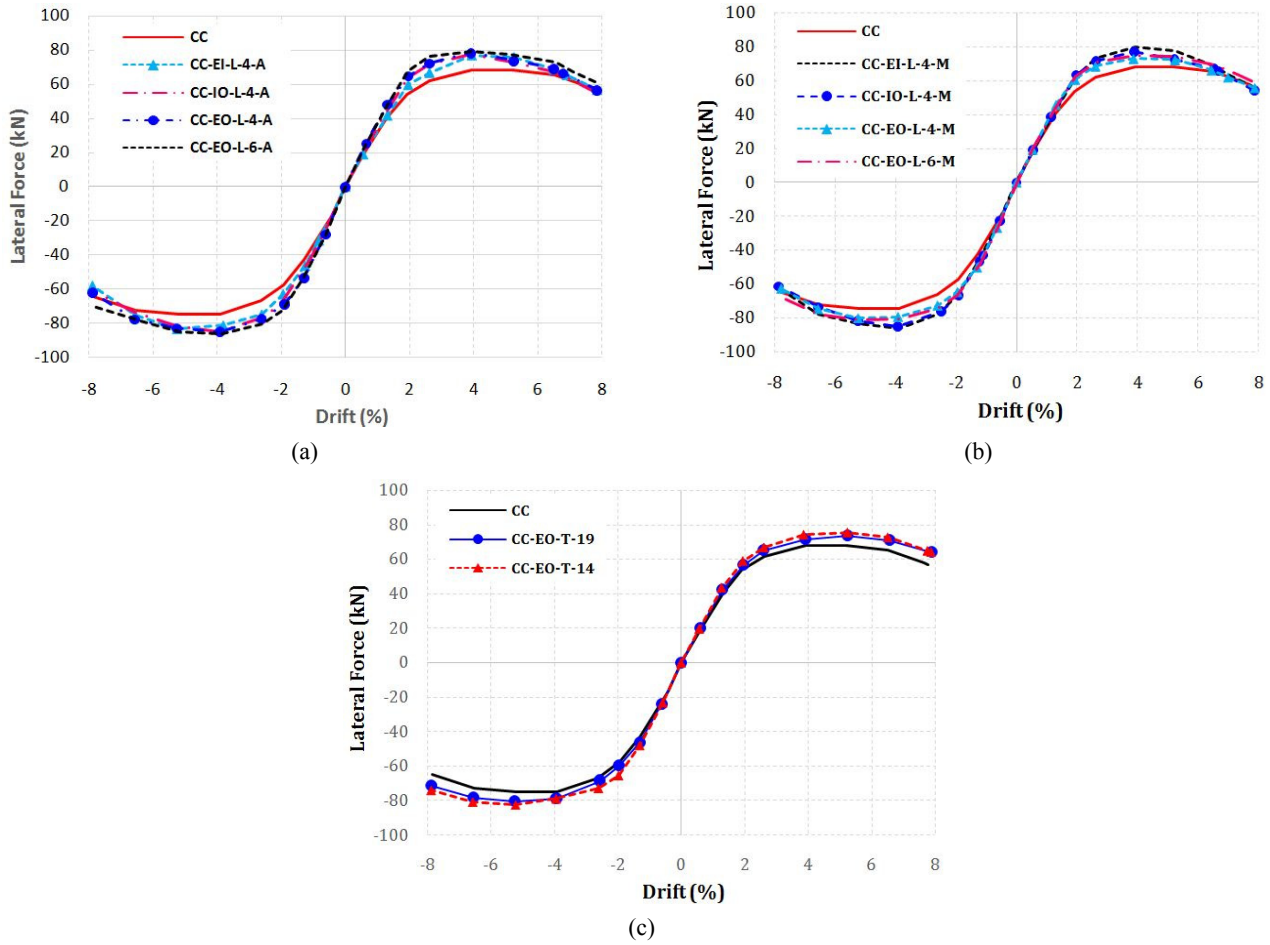


Fig. 18 Comparison between envelope curves of the models: (a) Longitudinally stiffened columns with the same cross-section area; (b) Longitudinally stiffened columns with the same moment of inertia; (c) Ring-stiffened columns

Table 4 Comparison of the initial stiffness, maximum lateral strength and strength degradation of the models

Column No.	Initial stiffness (K) (kN/m)	K. rel (kN/m)/(kN/m)	Max. strength (V_{max}) (kN)	V_{max} . rel (kN/kN)	Strength degradation (%)
CC	936.64	1	68.33	1.00	16.32
CC-EO-L-4-A	1122.14	1.2	78.43	1.15	29.57
CC-EO-L-6-A	1127.12	1.2	80.02	1.17	26.4
CC-IO-L-4-A	999.23	1.07	77.32	1.13	27.66
CC-EI-L-4-A	974.21	1.04	76.94	1.13	26.4
CC-EO-L-4-M	1034.54	1.1	72.92	1.07	31.82
CC-EO-L-6-M	1051.27	1.12	75	1.10	31.82
CC-IO-L-4-M	999.23	1.07	77.32	1.13	26.22
CC-EI-L-4-M	973.74	1.04	80.01	1.17	32.43
CC-EO-T-10	953.99	1.02	72.35	1.06	16.66
CC-EO-T-19	966.39	1.03	73.73	1.08	15.26
CC-EO-T-4	955.47	1.02	73.9	1.08	19.27
CC-EO-T-14	979.65	1.05	75.53	1.11	13.67

range of 2% up to 20%) compared to the unstiffened one subjected to combined axial and cyclic loads. The results also show the displacement ductility and energy-based ductility of models in the range of 5.08 to 5.55, and 13.39 to

15.84, respectively (Table 5). As given in Table 4, the lateral strength of CC-EO-L-4-M, CC-EO-L-6-M, CC-IO-L-4-M and CC-EI-L-4-M increase sequentially (i.e., 7%, 10%, 13% and 17%) compared to unstiffened CC column.

Table 5 Comparison of the energy dissipation, energy-based ductility and displacement-based ductility of the models

Column No.	Dissipated energy (E_{Diss}) (kJ)	E_{Diss} . rel (kJ)/(kJ)	Energy ductility (u_E) (%)	u_{E-rel}	Displacement ductility (u_D) (%)	u_{D-rel}
CC	63.36	1.00	15.84	1.00	5.57	1.00
CC-EO-L-4-A	107.32	1.69	13.39	0.85	5.16	0.93
CC-EO-L-6-A	107.55	1.70	14.65	0.92	5.42	0.97
CC-IO-L-4-A	95.76	1.51	14.02	0.89	5.09	0.91
CC-EI-L-4-A	76.34	1.20	15.26	0.96	5.25	0.94
CC-EO-L-4-M	92.3	1.46	13.8	0.87	5.55	1.00
CC-EO-L-6-M	94.11	1.49	15.53	0.98	5.33	0.96
CC-IO-L-4-M	95.76	1.51	14.02	0.89	5.08	0.91
CC-EI-L-4-M	86.23	1.36	15.82	1.00	5.33	0.96
CC-EO-T-10	65.55	1.03	17.45	1.10	6.09	1.09
CC-EO-T-19	64.5	1.02	17.53	1.11	6.16	1.11
CC-EO-T-4	83.8	1.32	17.08	1.08	5.9	1.06
CC-EO-T-14	85.5	1.35	17.41	1.10	6	1.08

The reasons for such differences can be explained through comparing the lateral stiffness of these models. Application of the stiffeners on the inner tube causes the moment of inertia and resulting lateral stiffness of the inner tube to be more than that of the outer tube.

The contribution portion of the inner tube on the lateral load carrying capacity is more than that of the outer tube, which in turn enhances lateral strength by delaying the onset of yielding and local buckling of the outer tube as well as crushing/cracking of the sandwiched concrete and lessening strength degradation of this model. Therefore, the column behaves more in an elastic manner leading to lower energy dissipation and lower ductility (Table 5).

As for the models with the same cross section area, higher lateral strength and energy dissipation of the columns with the stiffeners embedded on the outer tube are attributed to the anticipated role of outer tube in lateral load carrying capacity and yield initiation. Therefore, stiffening of outer tube with longitudinal stiffeners (i.e., CC-EO-L-4-M and CC-EO-L-6-M) improves the column behavior compared to that of inner tube (i.e., CC-EI-4-M). Delaying the onset of yielding and local buckling is identified as a major reason contributing to better performance of CC-EO-L-6-M and CC-EO-L-4-M models compared to CC one (Table 3). Note that for the models containing the same moment of inertia, consistently with observations made for the models with the same cross section area, models with 6 stiffeners behave better than those with 4 stiffeners. As illustrated in Table 5, CC-EO-L-4-M exhibits 13% and 15% less energy dissipation capacity than CC-EO-L-4-M and CC-IO-L-4-M, respectively. The closer spacing of longitudinal stiffeners serving as lateral bracing for the tubes would provide greater plastic deformation capacity because of postponing local buckling. Adding longitudinal stiffeners to the outer tube of CFDST columns with the same cross-section area and the counterparts with the same moment of inertia accentuates greater energy dissipation by as much as 70% and 51%, respectively. However,

embedding longitudinal stiffeners on the inner tube of the CFDST columns promotes energy dissipation up to 20% and 36% in the former and later cases, respectively. As can be seen in Table 4, the largest and smallest strength degradation in the CFDST columns with the same moment of inertia correspond to CC-IO-L-4-M and CC-EI-L-4-M with the amounts of 32.43% and 26.22%, respectively.

A brief summary of the lateral strength, energy dissipation and etc. of the ring stiffened CFDST columns is also provided in Tables 4 and 5. It is observed that the lateral strength, energy dissipation and elastic stiffness of the stiffened columns with ring stiffeners are more than that of unstiffened counterpart. This conclusion is further supported by comparison of the envelopes of hysteresis curves of the models in terms of lateral strength versus lateral displacement, shown in Fig. 18. Initial stiffness of ring stiffened CFDST columns is roughly 3% more than that of CC one. The lateral strength of CC-EO-T-10, CC-EO-T-19, CC-EO-T-4 and CC-EO-T-14 models is about 6%, 8%, 8% and 11% more than that of unstiffened one, respectively. Energy dissipation of uniform ring stiffened CFDST columns is only 3% more than that of CC model. However, by using the rings only at the critical position, the energy dissipation increases up to 35% more than that of CC one, indicating the ability of them to absorb significant amount of energy. As can be seen in Table 5, the uniformly distributed ring stiffeners have improving effect on the energy ductility and displacement ductility of the CFDST columns in a way that its value increases up to roughly 10% in comparison with that of CC model. The strength degradation of ring stiffened CFDST columns is comparable with that obtained with the unstiffened CC model.

3.3 Effects of different parameters on the cyclic behavior of the stiffened CFDST columns

3.3.1 Axial load ratio

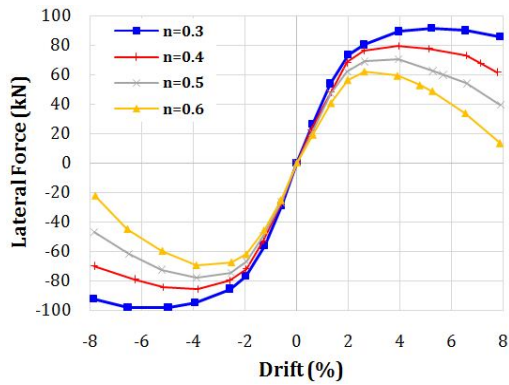
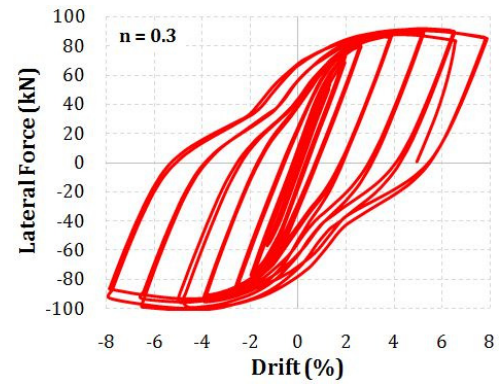


Fig. 19 Effect of load ratios on the envelope curves of CC-EO-L-6-A

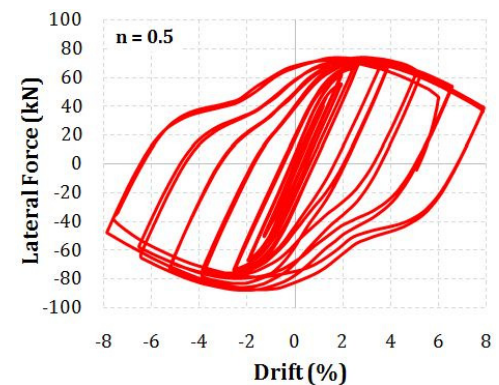
Table 6 Effect of load ratios on the performance characteristics of CC-EO-L-6-A

	Axial load ratio, n			
	0.3	0.4	0.5	0.6
Initial stiffness (K) (kN/m)	1233.38	1127.12	1011.82	891.24
K. rel (kN/m)/(kN/m)	1.00	0.91	0.82	0.72
Max. strength (V_{max}) (kN)	91.45	80.02	70.15	61.82
V_{max} . rel (kN/kN)	1.00	0.88	0.77	0.68
Strength degradation (%)	0.07	0.24	0.44	0.78
Dissipated energy (E_{Diss}) (kJ)	107.73	107.55	108.4	111.2
E_{Diss} . rel (kJ)/(kJ)	1.00	1.00	1.01	1.03
Energy ductility (u_E) (%)	17	14.64	10.13	8.34
u_E .rel	1.00	0.86	0.60	0.49
Displacement ductility (u_D) (%)	6.1	5.42	4.3	3.61
u_D .rel	1.00	0.89	0.70	0.59

Clearly, higher load level in the CFDST columns results in higher stress in concrete and steels subjected to cyclic loading. The main concern of this phase is to find an optimum axial compressive load level to use in seismic resistant design. Model CC-EO-L-6-A is taken for an example to illustrate the effect of axial compressive load level ranging from 0.3 to 0.6 on the seismic behavior of these columns. Fig. 19 shows the envelope hysteretic lateral load-displacement curve of CC-EO-L-6-A as a function of the axial compression load ratio. As can be seen in Table 6, the lateral strength of CC-EO-L-6-A decreases by as much as 9%, 18% and 28%, respectively, as the load level increases from 0.3 to 0.6. There is a reduction of 32%, 51% and 41% in the maximum lateral strength, energy-based ductility and displacement ductility of CC-EO-L-6-A as the axial load ratio increases from 0.3 to 0.6. As shown in Fig. 20, the hysteresis loops of the model CC-EO-L-6-A are plumper at the higher axial load ratios due to restriction imposed on the formation of opening and closing of the tensile crack. Therefore, although increasing axial load ratio would reduce the value of the maximum lateral strength of the column, it does not change the energy absorption



(a)



(b)

Fig. 20 Force-displacement hysteretic curves of CC-EO-L-6-A at load ratio of: (a) $n = 0.3$; (b) $n = 0.5$

capacity of that. As the load ratio increases from 0.3 to 0.6, the strength degradation of model approaches to 78% under cyclic loading.

3.3.2 End condition

For columns subjected to sidesway in an unbraced frame, two extreme cases are examined. On one extreme, if the bending stiffness of the beam approaches zero (Fig. 21(a)), the columns behave like a fixed-free member. On the other extreme, if the stiffness of the beam approaches infinity (Fig. 21(b)), the columns behave like a fixed-guided member. Fig. 22 shows the hysteresis curves generated from the lateral force versus drift ratio for CC, CC-EI-L-4-A and CC-EO-L-4-A columns containing fixed-guided end conditions. The buckling mode of CFDST columns with fixed-guided boundary condition under cyclic loading is sinusoidal in shape. As can be seen in Fig. 23, yielding and local buckling develop at both ends of columns.

Compared to similar hysteresis curves from the columns with fixed-free end condition, the excessive severity of the local buckling for columns with fixed-guided end condition is visible and accentuated the pinching of the CFDST columns. The envelopes of hysteresis curves of CC-EO-L-4-A having different end-conditions are illustrated in Fig. 24. Major differences as much as 368% and 157% in initial stiffness and maximum lateral strength, respectively, can be seen between models having fixed-free and fixed-guided end conditions, for either CC, CC-EI-L-4-A, or CC-EO-L-4-A. The maximum lateral strength, initial stiffness, energy

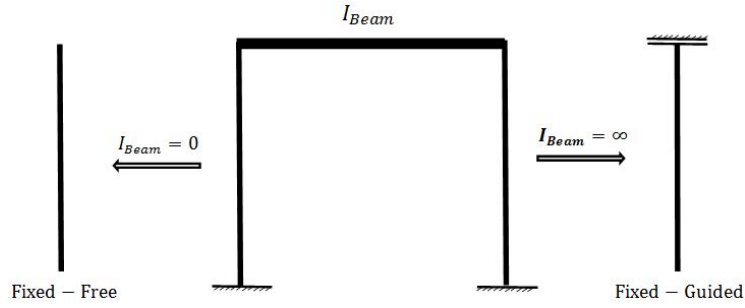


Fig. 21 Two extreme end conditions of columns in an unbraced frame

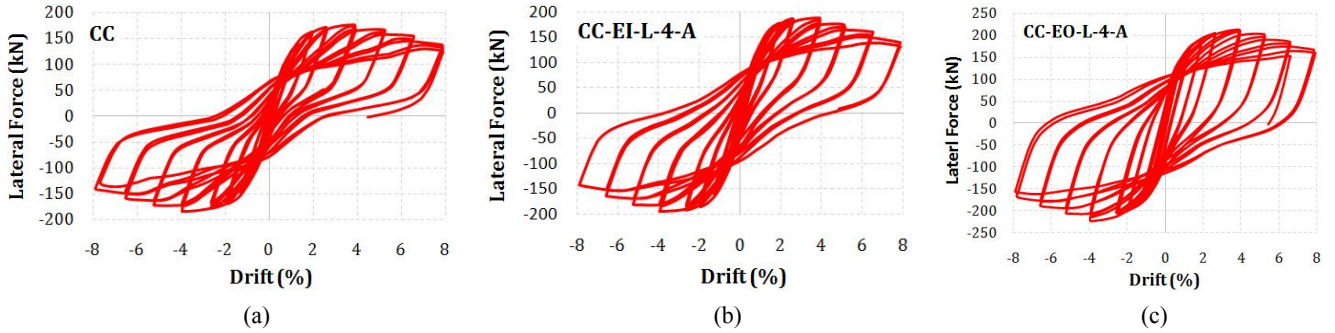


Fig. 22 Force-displacement hysteretic curves of the models containing fixed-guided end condition: (a) CC; (b) CC-EI-L-4-A; (c) CC-EO-L-4-A

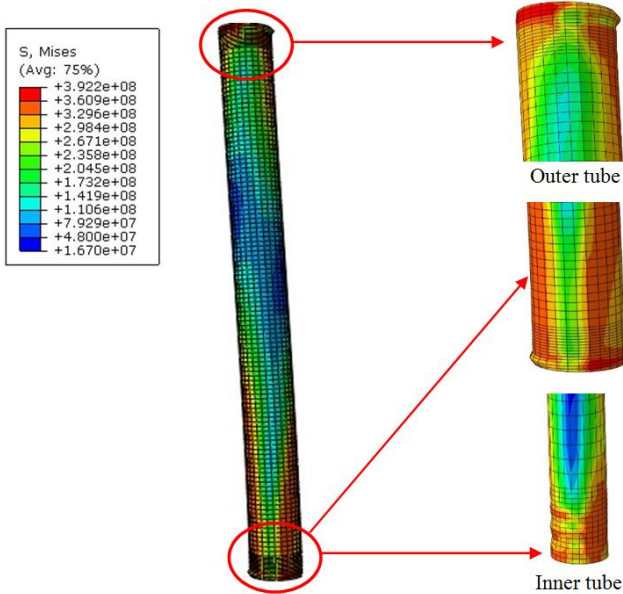


Fig. 23 Von-Mises stress distribution in CC containing fixed-guided end condition

dissipation capacity and ductility of the models with fixed-guided end condition are summarized in Table 7. As can be seen, stiffening CFDST columns by stiffeners in the exterior surface of inner tube has a similar trend on initial stiffness, lateral strength and energy dissipation compared to the previous end condition. However, the effect of longitudinal stiffeners embedded in the exterior surface of the outer tube is more pronounced for fixed-guided end condition. In the case of fixed-guided end condition, the initial stiffness,

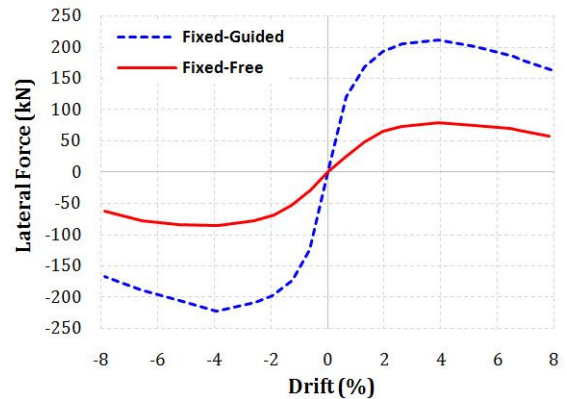


Fig. 24 Effect of end condition on the envelope curves of CC-EO-L-4-A

maximum lateral strength and energy dissipation capacity of CC-EO-L-4-A is more than those of CC by as much as 24%, 21% and 107%, respectively.

3.3.3 Hollow section ratio

The behavior of CFDST columns may be affected by the hollow ratio (χ) of the CFDST chord, as defined in Eq. (10)

$$\chi = \frac{D_i}{D_o - 2t_o} \quad (20)$$

The CC-EO-L-6-A model used to assess the effect of hollow section ratio is subjected to have a load ratio of 0.4 and hollow section ratios of 0.25, 0.5, and 0.75. Detailed information of the models is listed in Table 1. There is an increase in the concrete cross section area and consequently

Table 7 Effect of longitudinal stiffeners on the performance characteristics of CFDST columns in the case of fixed-guided end condition

	Initial stiffness (K) (kN/m)	K. rel (kN/m)/(kN/m)	Max. strength (V_{max}) (kN)	V_{max} . rel (kN/kN)	Strength degradation (%)	Dissipated energy (E_{Diss}) (kJ)	E_{Diss} . rel (kJ)/(kJ)	Energy ductility (u_E) (%)	u_E .rel	Displacement ductility (u_D) (%)	u_D .rel
CC	4332.37	1.00	175.4	1.00	0.22	144.72	1.00	32.3	1.00	10.68	1.00
CC-EI-L-4-A	4521.38	1.04	188.75	1.08	0.26	176.66	1.22	30.93	0.96	10.03	0.94
CC-EO-L-4-A	5355.79	1.24	211.4	1.21	0.22	299.12	2.07	31.76	0.98	10.65	1.00

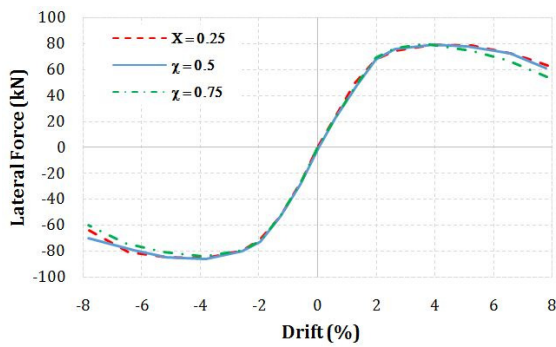


Fig. 25 Effect of hollow ratios on the envelope curves of CC-EO-L-6-A

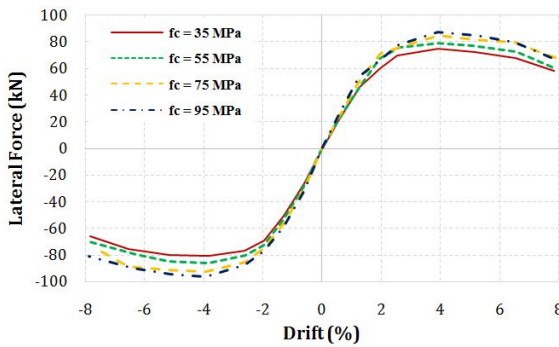


Fig. 26 Effect of concrete strength on the envelope curves of CC-EO-L-6-A

axial load demand on the model as the hollow section ratio decreases. The envelope curves of these models for lateral load versus lateral displacement results show no significant variation amongst each other, as shown in Fig. 25. By increasing the hollow section ratio, the initial stiffness of the model increases slightly by as much as 2%. Any increase in the column's hollow section ratio cause more parts of the inner and outer tubes to yield which in turn lead to small increase in the energy absorption capacity.

3.3.4 Concrete strength

Influence of concrete strength on the seismic behavior of the stiffened CFDST columns is realized through using characteristic strength of amount 35 MPa, 55 MPa, 75 MPa

Table 8 Effect of concrete strength on the performance characteristics of CC-EO-L-6-A

	Concrete strength (Mpa)			
	35	55	75	95
Initial stiffness (K) (kN/m)	1062.64	1127.12	1211.55	1272.46
K. rel (kN/m)/(kN/m)	1.00	1.06	1.14	1.20
Max. strength (V_{max}) (kN)	76.52	80.02	84.96	87.64
V_{max} . rel (kN/kN)	1.00	1.05	1.11	1.15
Strength degradation (%)	0.23	0.23	0.20	0.22
Dissipated energy (E_{Diss}) (kJ)	107.66	107.55	107.52	106.59
E_{Diss} . rel (kJ)/(kJ)	1.00	1.00	1.00	0.99
Energy ductility (u_E) (%)	14.65	14.64	15.3	14.52
u_E .rel	1.00	1.00	1.04	0.99
Displacement ductility (u_D) (%)	5.46	5.42	5.77	5.65
u_D .rel	1.00	0.99	1.06	1.03

and 95 MPa for concrete strength of the specimens. Fig. 26 illustrates lateral force-displacement envelopes of CC-EO-L-6-A specimen considering different concrete strength. Detailed information is given in Table 8. It is observed that the increases in concrete strength correspond to an increase in initial stiffness of the model by as much as 6%, 14% and 20% for concrete strength of 55, 75 MPa and 95 MPa, respectively, together with an increase of the maximum lateral strength equal to 42%, 51% and 56%, respectively. However, such concrete strength variations tend to have a negligible effect on the energy dissipation capacity and ductility of the model.

3.3.5 Discrete crack

In the current study, the discrete crack model is employed in the in-filled concrete to represent the major cracking behavior of the concrete. In Fig. 27, the hysteretic load-displacement curves of CC and CC-EO-L-4-A columns with and without inclusion of the discrete crack model are indicated. A comparison of lateral strength, initial stiffness, cumulative dissipated energy and ductility between models containing discrete crack and counterparts without discrete crack is given in Table 9. As can be seen,

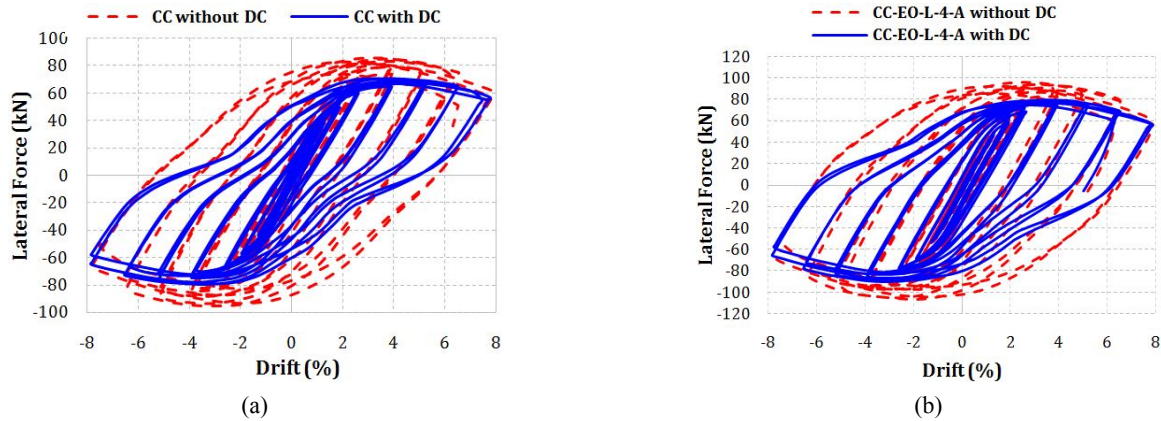


Fig. 27 Comparison of the hysteretic curves for models with and without inclusion of discrete crack (DC): (a) CC; (b) CC-EO-L-4-A

Table 9 Effect of concrete strength on the performance characteristics of CC-EO-L-6-A

	Initial stiffness (K) (kN/m)	K _{rel} (kN/m)/(kN/m)	Max. strength (V_{max}) (kN)	$V_{max, rel}$ (kN/kN)	Dissipated Energy (ED_{ISS}) (kJ)	$E_{Diss, rel}$ (kJ)/(kJ)
CC with DC	936.64	1.00	68.33	1.00	63.36	1.00
CC without DC	936.64	1.00	82.02	1.20	85.76	1.35
CC-EO-L-4-A with DC	1122.14	1.00	78.43	1.00	107.32	1.00
CC-EO-L-4-A without DC	1122.14	1.00	88.51	1.13	120.23	1.12

the models without the discrete crack simulation provide acceptable stiffness prediction but overestimate the actual strength and energy dissipation capacity by as much as 20% and 35%, respectively. It also failed to capture the pinching of the hysteretic curves for the CFDST columns under cyclic loading. It is found that the inclusion of the discrete crack model is inevitable since the crack behavior of the concrete cannot be accurately expressed by the concrete damaged plasticity model.

4. Conclusions

The main goal of the current research was to study the seismic behavior of longitudinal and transverse stiffened CFDST columns subjected to cyclic loading. The results of this study are used to obtain following conclusions regarding the prominent influence of stiffeners on the seismic performance of CFDST columns:

- The pinching behavior due to outer tube's local buckling and opening/closing of the major tensile crack is significantly improved with the addition of stiffeners. It is also found that the models with longitudinal stiffeners have plumper loop than the ones with ring stiffeners. The results indicate that

hysteretic curves of ring-stiffened CFDST columns become plumper with increase of transverse stiffeners at the critical positions prone to outer tube's local buckling;

- It is recommended that for improving the seismic performance of CFDST columns, the longitudinal stiffeners be welded to the exterior surface of the outer tubes. This method is more efficient than embedding longitudinal stiffeners to the inner tubes. Concerning the energy dissipation capacity, the columns stiffened by stiffeners employed on the outer tube show an increase up to 70% and 107% for fixed-free and fixed-guided end-conditions, respectively;
- The maximum energy-based ductility and displacement-based ductility predicted for stiffened CFDST columns are 17.5 and 6.15, respectively, corresponding to ring-stiffened CFDST columns. Generally, adding longitudinal stiffeners leads to a reduction of ductility compared with the respective unconfined CFDST column counterparts;
- Among the ring stiffening strategies, the use of rings only at the base of columns prone to the outer tube's local buckling appears to be an obvious and promising solution to strengthen CFDST columns. Ring stiffened CFDST columns exhibit 35% more energy dissipation capacity than that shown by the unstiffened counterpart;
- It was also found that variation of axial load ratio, hollow section ratio and concrete strength in stiffened CFDST columns does not show any further change in energy absorption of these models. However, the lateral strength and initial stiffness of stiffened CFDST columns decreases by as much as 32% and 28%, respectively, as the axial load ratio increases from 0.3 to 0.6;
- Local buckling of the steel tubes and subsequent strength degradation are observed when the cycling loading exceeded roughly 4% drift. Strength degradation is more significant for longitudinal stiffened CFDST columns compared to the ring-stiffened ones. As the hysteresis curves of models go through large drift ratio beyond 4%, large deforma-

tions in the inner tube resulting from the stiffeners directed in the load direction lead to more strength degradation.

References

- ABAQUS (2012), ABAQUS Standard User's Manual, Version 6.12.: Dassault Systèmes Corp., Providence, RI, USA.
- ACI (2008), Building code requirements for structural concrete and commentary; ACI 318-08, ACI.
- Ahmed, A.S., Ayman, H.H.K. and Osamma, H.A.W. (2005), "Response of concrete filled double skin steel tube columns to axial loads", *Proceedings of the 11th International Colloquium on Structural and Geotechnical Engineering*, 11(E05RC29), pp. 1-16.
- AISC (2010a), Specification for Structural Steel Buildings; ANSI/AISC 360-10, Chicago, IL, USA.
- AISC (2010b), Seismic Provisions for Structural Steel Buildings; ANSI/AISC 341, AISC, Chicago, IL, USA.
- ATC-24 (1992), Guidelines for Seismic testing of components of steel structures; Report 24, Applied, Redwood City, CA, USA.
- Dong, C.X. and Ho, J.C.M. (2012), "Uni-axial behaviour of normal-strength CFDST columns with external steel rings", *Steel Compos. Struct., Int. J.*, **13**(6), 587-606.
- Duarte, A.P.C., Silva, B.A., Silvestre, N., Brito, J. de, Julio, E., Castro, J.M. (2016), "Experimental study on short rubberized concrete-filled steel tubes under cyclic loading", *Compos. Struct.*, **136**, 394-404.
- Elchalakani, M., Zhao, X.L. and Grzebieta, R. (2002), "Tests on concrete-filled double-skin composite short columns under axial compression", *Thin Wall. Struct.*, **40**(5), 415-441.
- Espinos, A., Romero, M.L. and Hospitaler, A. (2010), "Advanced model for predicting the fire response of concrete filled tubular columns", *J. Constr. Steel Res.*, **66**, 1030-1046.
- Eurocode 4 (2005), Design of steel and concrete composite structures: part 1.2 general rules: structural fire design; EC4, Brussels, Belgium.
- FEMA (2009), Quantification of Building Seismic Performance Factors; FEMA P-695, USA.
- Goto, Y., Kumar, G.P. and Kawanishi, N. (2010), "Nonlinear Finite-Element Analysis for Hysteretic Behavior of Thin-Walled Circular Steel Columns with In-Filled Concrete", *J. Struct. Eng.*, **136**, 1413-1422.
- Han, L.H., Huang, H., Tao, Z. and Zhao, X.L. (2006), "Concrete-filled double skin steel tubular (CFDST) beam-columns subjected to cyclic bending", *Eng. Struct.*, **28**(12), 1698-1714.
- Han, L.H., Huang, H. and Zhao, X.L. (2009), "Analytical behaviour of concrete-filled double skin steel tubular (CFDST) beam-columns under cyclic loading", *Thin-Wall. Struct.*, **47**, 668-680.
- Han, T.H., Stallings, J.M. and Kang, Y.J. (2010), "Nonlinear concrete model for double-skinned composite tubular columns", *Constr. Build. Mater.*, **24**(12), 2542-2553.
- Han, L.H., Ren, Q.X. and Li, W. (2011), "Tests on stub stainless steel-concrete-carbon steel double-skin tubular (DST) columns", *J. Constr. Steel Res.*, **67**, 437-452.
- Hassanein, M.F., Kharoob, O.F. and Gardner, L. (2015), "Behaviour and design of square concrete-filled double skin tubular columns with inner circular tubes", *Eng. Struct.*, **100**, 410-424.
- Ho, J.C.M. and Dong, C.X. (2014), "Improving strength, stiffness and ductility of CFDST columns by external confinement", *Thin-Wall. Struct.*, **75**, 18-29.
- Hu, H.T. and Su, F.C. (2011), "Nonlinear analysis of short concrete-filled double skin tube columns subjected to axial compressive forces", *Marine Struct.*, **24**, 319-337.
- Imani, R., Mosqueda G. and Bruneau, M. (2014), "Post-Earthquake Fire Resistance of Ductile Concrete-Filled Double-Skin Tube Columns, Technical report", MCEER-14-0008.
- Imani, R., Mosqueda G. and Bruneau, M. (2015), "Finite Element Simulation of Concrete-Filled Double-Skin Tube Columns Subjected to Postearthquake Fires", *J. Struct. Eng.*, **141**(12), 04015055.
- Johansson, M. and Gylltoft, K. (2001), "Structural behavior of slender circular steel-concrete composite columns under various means of load application", *Steel Compos. Struct., Int. J.*, **1**(4), 393-410.
- Kim, J.K., Kwak, H.G. and Kwak, J.H. (2013), "Behavior of hybrid double skin concrete filled circular steel tube columns", *Steel Compos. Struct., Int. J.*, **14**(2), 191-204.
- Kojic, M. and Bathe, K.J. (2005), *Inelastic Analysis of Solids and Structures*, Springer.
- Lin, M.L. and Tsai, K.C. (2001), "Behavior of double-skinned composite steel tubular columns subjected to combined axial and flexural loads", *Proceedings of the 1st International Conference on Steel & Composite Structures*, pp. 1145-1152.
- Lu, H., Han, H.L. and Zhao, X.L. (2011), "FE modeling and fire resistance design of concrete filled double skin tubular columns", *J. Constr. Steel Res.*, **67**, 1733-1748.
- Mander, J.B., Priestley, M.J.N. and Park, R. (1988), "Theoretical stress-strain model for confined concrete", *J. Struct. Eng.*, **114**(8), 1804-1823.
- Nakanishi, K., Kitada, T. and Nakai, H. (1999), "Experimental study on ultimate strength and ductility of concrete filled steel columns under strong earthquakes", *J. Constr. Steel Res.*, **51**, 297-319.
- Pagoulatou, M., Sheehan, T., Dai, X.H. and Lam, D. (2014), "Finite element analysis on the capacity of circular concrete-filled double-skin steel tubular (CFDST) stub columns", *Eng. Struct.*, **72**, 102-112.
- Ren, Q.X., Hou, C., Lam, D. and Han, L.H. (2014), "Experiments on the bearing capacity of tapered concrete filled double skin steel tubular (CFDST) stub columns", *Steel Compos. Struct., Int. J.*, **17**(5), 667-686.
- Richart, F.E., Brandtzaeg, A. and Brown, R.L. (1928), "A study of the Failure of Concrete under Combined Compressive Stresses Bulletin", University of Illinois Engineering Experimental Station, Champaign, IL, USA, Volume 185.
- Romero, M.L., Espinos, A., Portolés, J.M., Hospitaler, A. and Ibañez, C. (2015), "Slender double-tube ultra-high strength concrete-filled tubular columns under ambient temperature and fire", *Eng. Struct.*, **99**, 536-545.
- Saenz, L.P. (1964), "Discussion of "Equation for the stress-strain curve of concrete", *ACI J.*, **61**, 1229-1235.
- Shekastehband, B., Taromi, A. and Abedi, K. (2017), "Fire performance of stiffened concrete filled double skin steel tubular columns", *Fire Safe. J.*, **88**, 13-25.
- Shimizu, M., Tatsumi, F., Ishikawa, T., Hattori, A. and Kawano, H. (2013), "Experimental study on ultimate strength of concrete filled double tubular steel with shear connector", *Int. J. Steel Struct.*, **13**(1), 49-54.
- Talaeitaba, S.B., Halabian, M. and Torki, M.E. (2015), "Nonlinear behavior of FRP-reinforced concrete-filled double-skin tubular columns using finite element analysis", *Thin-Wall. Struct.*, **95**, 389-407.
- Tao, Z., Han, L.H. and Zhao, X.L. (2004), "Behaviour of concrete-filled double skin steel tubular stub columns and beam-columns", *J. Constr. Steel Res.*, **60**(8), 1129-1258.
- Tao, Z., Wang, Z.B. and Yu, Q. (2013), "Finite element modelling of concrete-filled steel stub columns under axial compression", *J. Constr. Steel Res.*, **89**, 121-131.
- Zhao, X.L., Grzebieta, R.H. and Elchalakani, M. (2002), "Tests of

- concrete-filled double skin CHS composite stub columns”, *Steel Compos. Struct., Int. J.*, **2**(2), 129-142.
- Zhou, F. and Xu, W. (2016), “Cyclic loading tests on concrete-filled double-skin (SHS outer and CHS inner) stainless steel tubular beam-columns”, *Eng. Struct.*, **127**, 304-318.

DL